CHARLES UNIVERSITY IN PRAGUE

Faculty of Science

Doctoral thesis

Quantum computing approach to non-relativistic and relativistic molecular energy calculations

Libor Veis

Department of Physical and Macromolecular Chemistry

Supervisor: Mgr. Jiří Pittner, Dr. rer. nat.
Study programme: Physical chemistry

Prague, 2012

to my daughter Eliška

My momma always said,
„Life was like a box of chocolates. You never know what you’re gonna get.“
FORREST GUMP

Acknowledgement

I would like to thank my supervisor Dr. Jiří Pittner for the chance to work on such an interesting topic, his kind support, patience and encouragement.

I would also like to thank my friends Jirka Brabec and Marek Pederzoli for their enthusiasm and stimulating atmosphere in the office.

Last but not least, I would like to thank my loved wife Danuška, who has always stood by me, for her never-ending support that allowed me to finish this thesis. My great thanks also belong to my parents who have encouraged us (me and my brother) to learn new things all the time.

I acknowledge the financial support of the Czech Science Foundation (grant no. 203/08/0626), the Grant Agency of Charles University (grant no. 114310), and the Hlávka foundation.

Declaration

I declare that I carried out this doctoral thesis independently, and only with the cited sources, literature and other professional sources.

I understand that my work relates to the rights and obligations under the Act No. 121/2000 Coll., the Copyright Act, as amended, in particular the fact that the Charles University in Prague has the right to conclude a license agreement on the use of this work as a school work pursuant to Section 60 paragraph 1 of the Copyright Act.

October 23, 2012
Nučice
Libor Veis

Název práce: Nerelativistické a relativistické výpočty energií molekul na kvantových počítačích
Autor: RNDr. Libor Veis, Katedra fyzikální a makromolekulární chemie
Vedoucí disertační práce: Mgr. Jiří Pittner Dr. rer. nat., Ústav fyzikální chemie J. Heyrovského, AVČR

Abstrakt: Kvantové počítače umožňují řešit některé úlohy daleko rychleji než jejich klasické protějšky. Mohou například provádět přesné výpočty energií molekul metodou úplné konfigurační interakce (FCI) s pouze polynomiálním škálováním. To je v kontrastu s klasickými počítači, kde metoda FCI škáluje exponenciálně. Představujeme detailní popis kvantové verze metody FCI a výsledky numerických simulací výpočtů energií základního a excitovaných stavů methylénu. Dále jsme tuto metodu zobecnili pro relativistické čtyřsložkové výpočty a ukázali, jak efektivně řešit vlastní problém Diracova-Coulombova(-Breitova) Hamiltoniánu na kvantovém počítači. Funkčnost navrženého algoritmu byla ověřena numerickými simulacemi výpočtů hodnot spin-orbitálního štěpení molekuly SbH. Nakonec jsme navrhli 3-qubitové kvantové obvody s 9-ti a 10-ti CNOT hradly, které by mohly být vhodné pro experimentalní realizaci.

Klíčová slova: kvantová chemie, kvantové počítače, iterativní odhad fáze, methylén, multireferenční charakter, Diracův-Coulombův Hamiltonián, spin-orbitální štěpení, molekula SbH

Title: Quantum computing approach to non-relativistic and relativistic molecular energy calculations
Autor: Libor Veis, Department of physical and macromolecular chemistry
Supervisor: Dr. Jiří Pittner, J. Heyrovský institute of physical chemistry, ASCR

Abstract: Quantum computers are appealing for their ability to solve some tasks much faster than their classical counterparts. In fact, they have a potential to perform the full configuration interaction (FCI) energy calculations with a polynomial scaling only. This is in contrast to conventional computers where FCI scales exponentially. We provide a detailed description of the quantum version of the FCI method and the results of numerical simulations of the ground and excited state energy calculations of the methylene molecule. We further generalize this method to the relativistic four component regime and show how to efficiently solve the eigenproblem of the Dirac-Coulomb(-Breit) Hamiltonian on a quantum computer. We demonstrate the functionality of the proposed procedure by numerical simulations of computations of the spin-orbit splitting in the SbH molecule. Finally, we propose quantum circuits with 3 qubits and 9 or 10 CNOTs, which implement a proof-of-principle relativistic quantum chemical calculation for this molecule and might be suitable for an experimental realization.

Keywords: quantum chemistry, quantum computers, iterative phase estimation, methylene molecule, multireference character, Dirac-Coulomb Hamiltonian, spin-orbit splitting, SbH molecule

Contents

List of Figures 1

List of Tables 2

Introduction 5

1 Basics of quantum computing 9

- 1.1 Quantum bits . . . 9
  - 1.1.1 Multiple qubits . . . 10
  - 1.1.2 Entanglement . . . 11
- 1.2 Quantum circuit model . . . 12
  - 1.2.1 Single qubit gates . . . 13
  - 1.2.2 Two-qubit gates . . . 15
  - 1.2.3 Universal sets of quantum gates . . . 16
  - 1.2.4 Measurement . . . 18
- 1.3 Quantum parallelism . . . 19
- 1.4 Quantum computational complexity . . . 20
- 1.5 Physical realization of quantum computers . . . 22

2 Quantum algorithms 27

- 2.1 Quantum Fourier transform . . . 27
- 2.2 Semiclassical approach to quantum Fourier transform . . . 30
- 2.3 Phase estimation algorithm . . . 31
- 2.4 Iterative phase estimation algorithm . . . 34

3 Quantum full configuration interaction method 39

- 3.1 Mapping of quantum chemical wave functions onto quantum register . . . 39
- 3.2 Initial states for the algorithm . . . 40
  - 3.2.1 Adiabatic state preparation . . . 41

3.3 Controlled “time propagation” 41
3.3.1 Decomposition of unitary propagator to elementary quantum gates . . . 44

4 Non-relativistic example: methylene molecule 49
4.1 Introduction 49
4.2 Computational details 51
4.3 Results 52
4.3.1 C-H bond stretching 52
4.3.2 H-C-H angle bending 54
4.4 Discussion 55

5 Generalization to the relativistic four component regime 59
5.1 Relativistic electronic Hamiltonian 59
5.2 Relativistic qFCI algorithm 61
5.3 Relativistic example: the SbH molecule 63
5.3.1 Computational details 63
5.3.2 Results and discussion 64
5.4 Proof-of-principle experiment proposals 65

6 Conclusions 67

Appendices 69

A Probability analysis of the phase estimation algorithm 71

B Design of a quantum circuit for SbH proof-of-principle computation 73

List of shortcuts 77

List of Figures

1.1 Bloch sphere representation of a qubit. 10
1.2 Simple single qubit quantum circuit. 12
1.3 The action of the $R_y(\pi/2)$ rotation on the $|0\rangle$ state. 13
1.4 Hadamard gates change the sense of control and target qubits in case of the CNOT gate. 16
1.5 The Walsh-Hadamard transform. 20

2.1 The quantum Fourier transform circuit. 29
2.2 The SWAP gate by means of three CNOT gates. 29
2.3 Matrix representation of the controlled-R_j gate. 30
2.4 An alternative QFT circuit suitable for semiclassical simplifications. 30
2.5 Simplified, measurement based circuit for the kth qubit of the QFT. 31
2.6 The PEA circuit with the highlighted part corresponding to the inverse QFT. . . 32
2.7 The dependence of success probabilities of the PEA on δ for $m = 20$. 33
2.8 Example of the PEA circuit which recovers the second phase (see Table 2.1) of U (2.24) with unity probability. 34
2.9 The k-th iteration of the IPEA. 35
2.10 Comparison of the two versions of IPEA. 35
2.11 Energies of the four electronic states of H_2 in STO-3G basis which were obtained by the qFCI method (IPEA version **A**) with randomly generated initial guess states. 36

3.1 Adiabatic state preparation (ASP) of the SbH ground state for different internuclear distances. (a) Dependence of the IPEA success probability on time during the ASP. (b) Dependence of the energy gap between the ground and the first excited state on the adiabatic transition parameter. 42
3.2 The *exponential* speedup of the qFCI over the FCI. 47

4.1 (a) Energies of the four simulated states of CH_2 for the C-H bond stretching. (b) Energy of $\tilde{a}\ ^1A_1$ state of CH_2 for the H-C-H angle bending. 50
4.2 Success probabilities of the **A** version of IPEA for the four electronic states of CH_2 and different initial guesses. 52
4.3 Success probabilities of the **B** version of IPEA with HF guess for $\tilde{a}\ ^1A_1$ state and different number of repetitions of individual bit measurements. 54
4.4 Success probabilities of the **B** version of IPEA with “best” initial guesses and different number of repetitions of individual bit measurements for all four states. 55
4.5 Success probabilities of the **A** version of IPEA for the $\tilde{a}\ ^1A_1$ state with HF and CAS(2,2) initial guesses. 56
4.6 Success probabilities of the **B** version of IPEA with HF and CAS(2,2). 56

5.1 Simulated potential energy curves of ground (0^+) and excited (1) states of SbH, and spin-orbit energy splitting. 64
5.2 SbH ground (0^+) and excited (1) state qFCI success probabilities (SPs) corresponding to HF initial guesses. 65
5.3 Scheme of a circuit corresponding to CAS(4,3) calculations on SbH. 66

List of Tables

1.1 The quantum circuit model notation. 19

2.1 Eigenvalues, eigenvectors and corresponding phases of U (2.24). 34

4.1 Summary of the complete active spaces (CAS) used for the calculations of initial guesses for IPEA (Figures 4.2 and 4.4). 53

5.1 GAS and occupation constraints for SbH $X\ 0^+$ and $A\ 1$ states CI calculations. . 63

B.1 Circuit parameters for CAS(4,3) calculations of 0^+ and 1 states of SbH. 76

Introduction

An *exact* simulation of quantum systems on a classical computer is computationally hard. The problem lies in the dimensionality of the Hilbert space needed for the description of a studied system that in fact grows exponentially with the size of this system. No matter if we simulate the dynamics or calculate some static property e.g. the energy, this limitation is always present. Richard Feynman came up with an alternative to the classical simulation [1]. His idea was to convert the aforementioned drawback of quantum systems into their benefit. He suggested to map the Hilbert space of a studied quantum system on another one (both of them being exponentially large) and thus to *efficiently* simulate a quantum system on another one (i.e. on a quantum computer).

This was the original idea of quantum computers. There is no doubt that quantum computing is nowadays a well-established discipline of computer science. Apart from the *efficient* simulation of quantum systems [2, 3, 4, 5, 6], other interesting problems where quantum computers could beat their classical counterparts have been discovered. The most famous examples are integer factorization for which quantum computers supply an exponential speedup with respect to the best contemporary classical algorithm [7, 8] or database search with a quadratic speedup [9]. However, for the purposes of quantum chemistry and consequently for this thesis, the *efficient* (polynomially scaling) quantum algorithm of Abrams and Lloyd for obtaining eigenvalues of local Hamiltonians [10] is particularly important.

The first paper connecting quantum computation and chemistry was published by Lidar and Wang [11] and concerned the *efficient* calculations of thermal rate constants of chemical reactions. This work in fact founded the new field of computational chemistry, namely the "computational chemistry on quantum computers". Aspuru-Guzik et al. in their seminal article [12] reduced the number of quantum bits (qubits) needed by the Abrams and Lloyd's algorithm [10] and applied it to molecular ground state energy calculations. Since these two pioneering works, other papers involving energy calculations of excited states [13], quantum chemical dynamics [14], calculations of molecular properties and geometry optimizations [15], state preparations [16, 17] or global minima search [18] were published. The list of all chemical applications for quantum computers is quite rich and is very well reviewed in [19].

Aspuru-Guzik et al. [12] also proposed that quantum computers with tens of (noise free) qubits would already exceed the limits of classical full configuration interaction (FCI) calculations. This is in contrast to other quantum algorithms, e.g. the Shor's algorithm [7, 8] for integer factorization would for practical tasks in cryptography require thousands of qubits. For this reason, calculations and simulations of quantum systems will belong to the first practical applications of quantum computers. Recent proof-of-principle few-qubit experiments covering energy calculations of the hydrogen molecule [20, 21] or Heisenberg spin model [22] and the simulation of a chemical reaction dynamics [23] confirm that interesting applications might be just behind the door.

The aim of this thesis is to summarize our work on a quantum[1] version of the FCI method (qFCI) and its simulations [24, 25, 26]. On a classical computer, a computational cost of the FCI method scales exponentially with the size of the system. This fact stems from the dimension of the Hilbert space in which we diagonalize the Hamiltonian matrix and it is the reason why this method is limited only to the smallest systems (diatomics, triatomics). For example, in the non-relativistic case, the number of Slater determinants that build up the FCI wave function for a closed-shell system with n electrons in m orbitals[2] is equal to

$$N_{\mathrm{non-rel.}} = \begin{pmatrix} m \\ n/2 \end{pmatrix}^2 . \tag{1}$$

It is more than evident that this number grows into huge values with increasing m and n very quickly. On a quantum computer on the other hand, it has been shown [20, 27] and will be discussed in Chapter 3 that the qFCI cost has a polynomial scaling [$\mathcal{O}(m^5)$], therefore it is *exponentially* faster.

The thesis is organized as follows. It starts with an introduction to the quantum computation in Chapter 1. Most importantly, the quantum cirucit model, which is used throughout the thesis, is presented here. This chapter is closed with the section devoted to a physical realization of quantum computers. Chapter 2 deals with quantum algorithms that are important in the context of the quantum full configuration interaction method, namely the quantum Fourier transform (Section 2.1), the phase estimation algorithm (Section 2.3) and its iterative version (Section 2.4). The quantum full configuration interaction (qFCI) method is presented in detail in Chapter 3. Chapter 4 discusses classical simulations of non-relativistic qFCI calculations of methylene molecule whose lowest lying singlet electronic states exhibit multireference character. In Chapter 5, we generalize the qFCI method to the relativistic (4-component, no-pair) regime and test its performance on the spin-orbit splitting of the SbH molecule.

---

[1] Here „quantum“ denotes quantum computing.

[2] We simply take into account all determinants with the same number of alpha and beta electrons equal to $n/2$ ($M_S = 0$).

Several chapters of this thesis are based on results published in the following papers/book chapters:

- L. Veis and J. Pittner, Quantum computing applied to calculations of molecular energies: CH_2 benchmark, *J. Chem. Phys.*, **133**, 194106, (2010) also selected for the December 2010 issue of *Virtual Journal of Quantum Information* (Chapter 4).
- L. Veis, J. Višňák, T. Fleig, S. Knecht, T. Saue, L. Visscher, and J. Pittner, Relativistic quantum chemistry on quantum computers, *Phys. Rev. A*, 85, 030304(R), (2012) (Chapter 5).
- L. Veis and J. Pittner, Quantum computing approach to non-relativistic and relativistic molecular energy calculations, *Advances in Chemical Physics* (2012), in press, preprint available: arXiv:1203.6204 (Chapters 2 and 3).

1 Basics of quantum computing

In this chapter, we give a brief introduction to the field of quantum computation [28] that may be useful especially for readers coming from the quantum chemistry community.

1.1 Quantum bits

Similarly as the fundamental entity of classical computation and classical information is one *bit*, the fundamental entity of quantum computation and quantum information is one *quantum bit*, shortly *qubit*. It is a quantum two-state system in a normalized state

$$|\psi\rangle = \alpha|0\rangle + \beta|1\rangle, \tag{1.1}$$

where α and β are complex-valued amplitudes. The examples of physical realization can be a polarization of a photon with two distinct polarization states or an electron in an external magnetic field with two different spin directions. A bit more details about some of the examples of physical realization of quantum computing are mentioned in Section 1.5.

The orthonormal basis $\mathcal{B} = \{|0\rangle, |1\rangle\}$, which is usually denoted as a *computational basis*, is defined as

$$|0\rangle = \begin{pmatrix} 1 \\ 0 \end{pmatrix}, \quad |1\rangle = \begin{pmatrix} 0 \\ 1 \end{pmatrix}, \tag{1.2}$$

therefore

$$|\psi\rangle = \begin{pmatrix} \alpha \\ \beta \end{pmatrix}. \tag{1.3}$$

Because $|\alpha|^2 + |\beta|^2 = 1$, we may rewrite (1.1) as

$$|\psi\rangle = e^{i\gamma}\Big(\cos\frac{\theta}{2}|0\rangle + e^{i\varphi}\sin\frac{\theta}{2}|1\rangle\Big), \tag{1.4}$$

where θ, φ and γ are real numbers. As the global phase $e^{i\gamma}$ is not observable [28], we can effectively write

$$|\psi\rangle = \cos\frac{\theta}{2}|0\rangle + e^{i\varphi}\sin\frac{\theta}{2}|1\rangle. \tag{1.5}$$

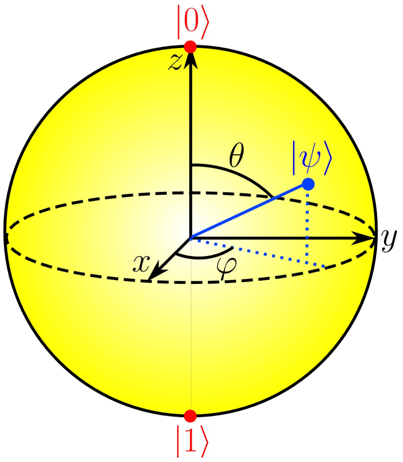

Figure 1.1: Bloch sphere representation of a qubit.

Geometrically, the numbers θ and φ define a point on the unit three-dimensional sphere, often called the Bloch sphere (see Figure 1.1), and a general single qubit's state can be viewed as a point on this sphere. This graphical representation is a very elegant and useful concept. However, it must be noted that there is no simple generalization of the Bloch sphere known for multiple qubits.

The Bloch sphere representation of a single qubit can be generalized to mixed states. An arbitrary density matrix of a single qubit may be written as

$$\rho = \frac{I + \vec{r}\cdot\vec{\sigma}}{2} \tag{1.6}$$

where $\vec{\sigma}$ is a vector of Pauli matrices (see Eq. 1.14) and $\vec{r}$ is a real three-dimensional Bloch vector such that $\|\vec{r}\| \leq 1$.

1.1.1 Multiple qubits

When going to multiple qubits, the computational basis increases exponentially. For example, a two qubit system has four computational basis states

$$|00\rangle = \begin{pmatrix} 1 \\ 0 \end{pmatrix} \otimes \begin{pmatrix} 1 \\ 0 \end{pmatrix} = \begin{pmatrix} 1 \\ 0 \\ 0 \\ 0 \end{pmatrix}, \quad |01\rangle = \begin{pmatrix} 1 \\ 0 \end{pmatrix} \otimes \begin{pmatrix} 0 \\ 1 \end{pmatrix} = \begin{pmatrix} 0 \\ 1 \\ 0 \\ 0 \end{pmatrix},$$

$$|10\rangle = \begin{pmatrix} 0 \\ 1 \end{pmatrix} \otimes \begin{pmatrix} 1 \\ 0 \end{pmatrix} = \begin{pmatrix} 0 \\ 0 \\ 1 \\ 0 \end{pmatrix}, \quad |11\rangle = \begin{pmatrix} 0 \\ 1 \end{pmatrix} \otimes \begin{pmatrix} 0 \\ 1 \end{pmatrix} = \begin{pmatrix} 0 \\ 0 \\ 0 \\ 1 \end{pmatrix} \tag{1.7}$$

and a general two qubit's state has the form

$$|\psi\rangle = \alpha|00\rangle + \beta|01\rangle + \gamma|10\rangle + \delta|11\rangle. \tag{1.8}$$

Obviously, the Hilbert space spanned by all possible states of a quantum register consisting of n qubits will be 2^n-dimensional.

1.1.2 Entanglement

An interesting property that follows from the postulates of quantum mechanics is the *entanglement*. In fact, there exist such states of composite systems that cannot be written as a tensor product of states of its component systems. They are called *entangled*. One of many examples is the Bell state

$$\beta_{00} = \frac{|00\rangle + |11\rangle}{\sqrt{2}}. \tag{1.9}$$

To show that it is entangled, let's firstly suppose the opposite. If it was not entangled, it should be possible to write it as a product state

$$\beta_{00} = |\varphi\rangle \otimes |\psi\rangle, \tag{1.10}$$

where

$$\begin{aligned} |\varphi\rangle &= \alpha|0\rangle + \beta|1\rangle, \\ |\psi\rangle &= \gamma|0\rangle + \delta|1\rangle. \end{aligned} \tag{1.11}$$

However, this is clearly not possible, as the following conditions for β_{00} (1.9) amplitudes cannot be fulfilled simultaneously

$$\begin{aligned} \alpha\gamma &= \frac{1}{\sqrt{2}}, & \alpha\delta &= 0, \\ \beta\gamma &= 0, & \beta\delta &= \frac{1}{\sqrt{2}}. \end{aligned} \tag{1.12}$$

In entangled states, unitary operators and measurements performed on one system affect the state of the second system. Entangled states can mediate correlations of space-like separated measurements, however they cannot be used to transmit information faster then light. This remains a very intriguing and still not completely understood feature of quantum mechanics.

Entangled states play a crucial role in quantum computation and quantum information. For example the aforementioned β_{00} state is a key ingredient for quantum teleportation or superdense coding [28].

1.2 Quantum circuit model

There exist several models of quantum computation that are mutually equivalent. One of them used in this thesis is the *quantum circuit model* [29]. Analogously to a classical computation which is implemented with electrical circuits containing logical gates connected by wires, quantum computation can be implemented with a quantum circuit containing "wires" and quantum gates, which manipulate the quantum information.

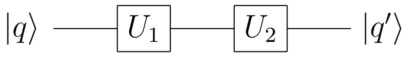

Figure 1.2: Simple single qubit quantum circuit. The time flows from left to right.

An example of a simple single qubit quantum circuit is shown in Figure 1.2. By convention, in quantum circuits the time flows from left to right, i.e. the qubit is originally in the state $|q\rangle$ and after action of quantum gates U_1 and U_2, it is transformed onto $|q'\rangle$. Algebraically, it can be written as

$$|q'\rangle = U_2 U_1 |q\rangle. \tag{1.13}$$

According to the postulates of quantum mechanics [30], the time evolution of a quantum system must be unitary, i.e. quantum gates (operations on qubits) must be unitary operators. An important consequence of quantum mechanics is so called *no-cloning* theorem [28] which states that it is not possible to make a copy of an unknown quantum state.

1.2.1 Single qubit gates

Operations on a single qubit are represented by 2×2 unitary matrices. Between the most important ones belong the Pauli matrices

$$\sigma_x \equiv X = \begin{pmatrix} 0 & 1 \\ 1 & 0 \end{pmatrix}, \quad \sigma_y \equiv Y = \begin{pmatrix} 0 & -i \\ i & 0 \end{pmatrix}, \quad \sigma_z \equiv Z = \begin{pmatrix} 1 & 0 \\ 0 & -1 \end{pmatrix}. \tag{1.14}$$

The Pauli matrices when exponentiated give rise to rotation operators about x, y and z axes, defined by the equations

$$R_x(\theta) = e^{-i\theta X/2} = \cos\frac{\theta}{2} I - i \sin\frac{\theta}{2} X = \begin{pmatrix} \cos\frac{\theta}{2} & -i\sin\frac{\theta}{2} \\ -i\sin\frac{\theta}{2} & \cos\frac{\theta}{2} \end{pmatrix} \tag{1.15}$$

$$R_y(\theta) = e^{-i\theta Y/2} = \cos\frac{\theta}{2} I - i \sin\frac{\theta}{2} Y = \begin{pmatrix} \cos\frac{\theta}{2} & -\sin\frac{\theta}{2} \\ \sin\frac{\theta}{2} & \cos\frac{\theta}{2} \end{pmatrix} \tag{1.16}$$

$$R_z(\theta) = e^{-i\theta Z/2} = \cos\frac{\theta}{2} I - i \sin\frac{\theta}{2} Z = \begin{pmatrix} e^{-i\frac{\theta}{2}} & 0 \\ 0 & e^{i\frac{\theta}{2}} \end{pmatrix}, \tag{1.17}$$

where I is the identity matrix

$$I = \begin{pmatrix} 1 & 0 \\ 0 & 1 \end{pmatrix}. \tag{1.18}$$

The fact that they behave like rotations can be viewed in the Bloch sphere picture. We demonstrate it in Figure 1.3 on the example of $R_y(\pi/2)$ rotation which transforms $|0\rangle$ onto $\frac{|0\rangle+|1\rangle}{\sqrt{2}}$.

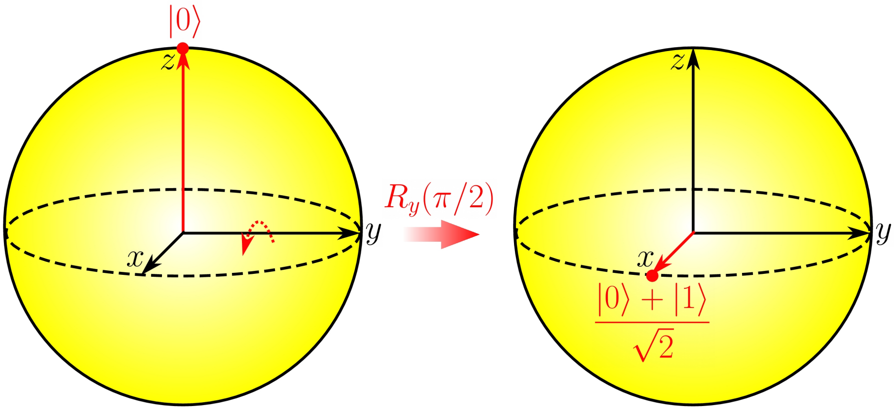

Figure 1.3: The action of the $R_y(\pi/2)$ rotation on the $|0\rangle$ state.

Other important single qubit gates that appear very often in quantum circuits are the Hadamard gate

$$H = \frac{1}{\sqrt{2}} \begin{pmatrix} 1 & 1 \\ 1 & -1 \end{pmatrix}, \tag{1.19}$$

with the following action on a computational basis

$$\begin{aligned} H|0\rangle &\longrightarrow \frac{1}{\sqrt{2}}\Big(|0\rangle + |1\rangle\Big) \\ H|1\rangle &\longrightarrow \frac{1}{\sqrt{2}}\Big(|0\rangle - |1\rangle\Big), \end{aligned} \tag{1.20}$$

the $\pi/8$ gate (denoted T), and the phase gate (denoted S):

$$T = \begin{pmatrix} 1 & 0 \\ 0 & e^{i\pi/4} \end{pmatrix}, \qquad S = \begin{pmatrix} 1 & 0 \\ 0 & i \end{pmatrix}. \tag{1.21}$$

An arbitrary unitary single qubit operation can be implemented with two rotations of the Bloch sphere about z axis and one about y axis [28]:

$$U = e^{i\alpha} R_z(\beta) R_y(\gamma) R_z(\delta) \qquad\qquad (Z\text{-}Y \text{ decomposition}) \tag{1.22}$$

and therefore parametrized by four real numbers α, β, γ and δ. In fact, the choice of y and z axes is not unique and for an arbitrary single qubit gate holds

$$U = e^{i\alpha} R_{\hat{n}}(\beta) R_{\hat{m}}(\gamma) R_{\hat{n}}(\delta), \tag{1.23}$$

where $\hat{m}$ and $\hat{n}$ are non-parallel unit vectors in the three-dimensional Euclidian space.

There exist plenty of single qubit circuit identities [28]. We picked up only few of them that are frequently used when working with quantum circuits:

$$HXH = Z \tag{1.24}$$

$$HYH = -Y \tag{1.25}$$

$$HZH = X \tag{1.26}$$

$$HTH = e^{i\pi/8} R_x(\pi/4) \tag{1.27}$$

$$XYX = -Y \tag{1.28}$$

$$XR_y(\theta)X = R_y(-\theta) \tag{1.29}$$

$$XZX = -Z \tag{1.30}$$

$$XR_z(\theta)X = R_z(-\theta) \tag{1.31}$$

1.2.2 Two-qubit gates

Two-qubit gates are represented by 4×4 unitary matrices. By two-qubit gates we mean only operations over two qubits that *cannot* be decomposed to single qubit gates. A special class of two-qubit gates are controlled single qubit operations. These are gates with two input (and also output) qubits, known as the *control qubit* and *target qubit*, respectively. The action of a general two-qubit controlled-U operation in terms of the computational basis is the following: if the control qubit is in the $|0\rangle$ state then U is applied to the target qubit, otherwise the target qubit is left alone; that is, $|c\rangle|t\rangle \longrightarrow |c\rangle U^c|t\rangle$.

In this thesis, we adopt the usual convention that the top-most qubit in a circuit corresponds to the left-most qubit in a ket:

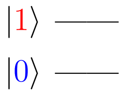

$$= |1\rangle \otimes |0\rangle = |10\rangle. \tag{1.32}$$

Using this convention, the controlled-U gate has the following block-diagonal structure[1].

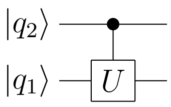

$$= \begin{pmatrix} 1 & 0 & 0 & 0 \\ 0 & 1 & 0 & 0 \\ 0 & 0 & \boxed{U_{11}} & \boxed{U_{12}} \\ 0 & 0 & \boxed{U_{21}} & \boxed{U_{22}} \end{pmatrix} \begin{array}{c} |q_2q_1\rangle \\ \begin{pmatrix} \alpha \ldots |00\rangle \\ \beta \ldots |01\rangle \\ \gamma \ldots |10\rangle \\ \delta \ldots |11\rangle \end{pmatrix} \end{array}$$

The prototypical two-qubit gate is the controlled-NOT (CNOT) with the matrix representation

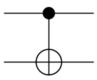

$$= \begin{pmatrix} 1 & 0 & 0 & 0 \\ 0 & 1 & 0 & 0 \\ 0 & 0 & 0 & 1 \\ 0 & 0 & 1 & 0 \end{pmatrix}$$

and action in the computational basis

$$|00\rangle \longrightarrow |00\rangle; \quad |01\rangle \longrightarrow |01\rangle; \quad |10\rangle \longrightarrow |11\rangle; \quad |11\rangle \longrightarrow |10\rangle. \tag{1.33}$$

Another way of describing the CNOT is a generalization of the classical XOR gate, since the action of the gate may be summarized as $|A, B\rangle \longrightarrow |A, B \oplus A\rangle$, where $\oplus$ is addition modulo two, which is exactly what the XOR gate does [28].

---

[1] For convenience, a general two-qubit state vector $(\alpha\, \beta\, \gamma\, \delta)^T$ on which the matrix acts and also corresponding computational basis states are shown.

The division of qubits into control and target can sometimes be misleading as is shown in Figure 1.4 on the example of the CNOT gate. One can easily verify that Hadamard gates lead to the exchange of control.

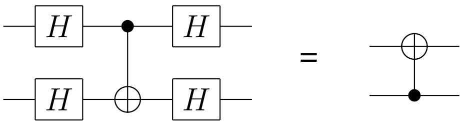

Figure 1.4: Hadamard gates change the sense of control and target qubits in case of the CNOT gate.

1.2.3 Universal sets of quantum gates

The CNOT gate is prototypical for several reasons. Firstly, its action is relatively easy to understand [2], and moreover, there is a simple proof (see bellow) that an arbitrary controlled single qubit gate can be constructed using at most two CNOTs and three single qubit gates.

Let U be a single qubit gate. Then there exist single qubit gates A, B, C such that $ABC = I$ and $U = AXBXC$. Controlled-U is then implemented by the following circuit.

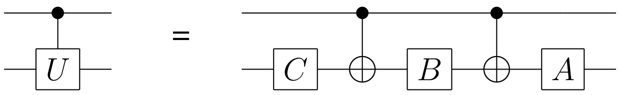

The proof is constructive. Up to the global phase, $U = R_z(\alpha)R_y(\beta)R_z(\gamma)$ for some α, β, $\gamma \in \mathbb{R}$ (see Eq. 1.22). Set $A = R_z(\alpha)R_y(\beta/2)$, $B = R_y(-\beta/2)R_z(-(\alpha+\gamma)/2)$ and $C = R_z((-\alpha+\gamma)/2)$. Then

$$ABC = R_z(\alpha)\underbrace{R_y(\beta/2)R_y(-\beta/2)}_{I}\overbrace{R_z(-(\alpha+\gamma)/2)R_z((-\alpha+\gamma)/2)}^{R_z(-\alpha)} = I.$$

Using the identity $I = XX$ and Eqs. 1.29 and 1.31,

$$\begin{aligned}
AXBXC &= R_z(\alpha)R_y(\beta/2)XR_y(-\beta/2)R_z(-(\alpha+\gamma)/2)XR_z((-\alpha+\gamma)/2)\\
AXBXC &= R_z(\alpha)R_y(\beta/2)\underbrace{XR_y(-\beta/2)(X}_{R_y(\beta/2)}\overbrace{X)R_z(-(\alpha+\gamma)/2)X}^{R_z((\alpha+\gamma)/2)}R_z((-\alpha+\gamma)/2)\\
AXBXC &= R_z(\alpha)R_y(\beta)R_z(\gamma).
\end{aligned}$$

---

[2] However, as Figure 1.4 indicates, it has also some surprising properties.

It is not only the controlled-U that can be build from CNOTs and single qubit gates indeed. Barenco *et al.* [31] showed that an *arbitrary* n-qubit gate can be constructed solely from single qubit gates and CNOTs. Single qubit gates then can be build e.g. from y and z rotations according to Eq. (1.22).

The number of CNOTs basically describes the length of a circuit (only one single qubit gate makes sense between two successive CNOTs) and also complexity of its physical realization (their implementations are orders of magnitude more difficult than implementations of single qubit gates). Obviously, it is desirable to minimize the number of CNOTs (or other two-qubit gates) when designing quantum circuits.

Finite universal sets of quantum gates

In what follows, we will show that the set {CNOT, H, T} is universal in the sense that any n-qubit gate can be arbitrarily accurately approximated using only gates from this set. Because we have already mentioned that CNOTs together with single qubit gates are universal, it remains to show that any single qubit gate can be arbitrarily accurately approximated using only Hadamard and $\pi/8$ (T) gates.

Using (1.27), up to an unimportant global phase, it holds

$$\begin{aligned} HTHT &= R_x(\pi/4)R_z(\pi/4) = e^{-i(\pi/8)X}e^{-i(\pi/8)Z} = \\ &= \Big(\cos\frac{\pi}{8}I - i\sin\frac{\pi}{8}X\Big)\Big(\cos\frac{\pi}{8}I - i\sin\frac{\pi}{8}Z\Big) = \\ &= \cos^2\frac{\pi}{8}I - i\Big(\cos\frac{\pi}{8}(X+Z) + \sin\frac{\pi}{8}Y\Big)\sin\frac{\pi}{8} = R_{\hat{n}}(\theta_C). \end{aligned} \tag{1.34}$$

$R_{\hat{n}}(\theta_C)$ represents a rotation of the Bloch sphere about an axis along $\vec{n} = (\cos\frac{\pi}{8}, \sin\frac{\pi}{8}, \cos\frac{\pi}{8})$ through an angle θ_C defined by

$$\cos\frac{\theta_C}{2} = \cos^2\frac{\pi}{8}. \tag{1.35}$$

It can be shown that θ_C is an irrational multiple of 2π [32] and due to this fact repeated iteration of $R_{\hat{n}}(\theta_C)$ can be used to approximate to arbitrary accuracy any rotation $R_{\hat{n}}(\alpha)$ [28].

Similarly,

$$HR_{\hat{n}}(\alpha)H = THTH = R_{\hat{m}}(\alpha), \tag{1.36}$$

where $\hat{m}$ is a unit vector along $\vec{m} = (\cos\frac{\pi}{8}, -\sin\frac{\pi}{8}, \cos\frac{\pi}{8})$. When looking at (1.23), we can conclude that any single qubit gate can be constructed only from Hadamard and $\pi/8$ gates.

The aforementioned finite universal set of quantum gates is in fact not unique. Several other equivalent ones have been discovered, e.g. {Controlled-S,H}. An important criterion of these sets is whether their gates can operate fault-tolerantly. The fault-tolerance is a concept arising in the context of *quantum error correction* (QEC) [33]. In QEC, one works with logical qubits encoded on more physical qubits. This approach is resistant to some sort of errors that can be corrected during the computation. The QEC requires gates to operate fault-tolerantly, i.e. an error on a single physical qubit cannot propagate to other physical qubits in the same logical unit. We close this part with the statement that both of the sets {CNOT,H,T} and {Controlled-S,H} are fault-tolerant.

1.2.4 Measurement

A final element of quantum circuits is always a measurement that reveals some information. According to the postulates of quantum mechanics [30], measurement is destructive, because it destroys superpositions. In particular, let $\mathcal{H}$ be a Hilbert space spanned by the basis $\mathcal{B}$, then a projective measurement associated with some observable

$$M = \sum_m r_m P_m, \tag{1.37}$$

where P_m are orthogonal projectors

$$P_m = |m\rangle\langle m|, \quad |m\rangle \in \mathcal{B}, \tag{1.38}$$

projects the state $|\psi\rangle = \sum_i \alpha_i |i\rangle$, where $|i\rangle \in \mathcal{B}$ onto the state

$$|\psi_{\text{final}}\rangle = \frac{P_m|\psi\rangle}{\sqrt{p(r_m)}} = \frac{1}{|\alpha_m|}\sum_i \alpha_i |m\rangle\langle m|i\rangle = \frac{1}{|\alpha_m|}\sum_i \alpha_i |m\rangle \delta_{mi} = \frac{\alpha_m}{|\alpha_m|}|m\rangle, \tag{1.39}$$

with probability

$$p(r_m) = \langle\psi|P_m|\psi\rangle = |\alpha_m|^2. \tag{1.40}$$

Outcome of the measurement is r_m and $\frac{\alpha_m}{|\alpha_m|}$ corresponds to a global phase which is not measurable. In principle, it is possible to measure only part of the register, e.g. only one qubit. In such a case, when working with entangled states, the whole register is affected.

We close this section with Table 1.1 which summarizes the quantum circuit model notation that is used throughout this thesis.

wire carrying a qubit	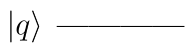
measurement: projection onto $\|0\rangle$ and $\|1\rangle$	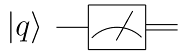
unitary operation U	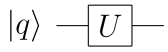
controlled-U operation	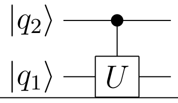
controlled-NOT operation	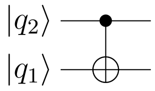

Table 1.1: The quantum circuit model notation.

1.3 Quantum parallelism

Quantum parallelism is a fundamental feature of many quantum algorithms [28] and is often mentioned as a source of power of quantum computers. It follows from the dimensionality of the Hilbert space of a quantum register and from the fact that unitary operators are linear.

We show its performance on the example of a function evaluation. Quantum computers can actually evaluate a function $f(x)$ for many different values of x simultaneously. Let for simplicity $f(x)$ be a function with n-bit input and only one-bit output:

$$f(x) : \{0,1\}^{\otimes n} \longrightarrow \{0,1\} \tag{1.41}$$

and U_f unitary operator with a mapping

$$U_f : |x, y\rangle \longrightarrow |x, y \oplus f(x)\rangle, \tag{1.42}$$

where $\oplus$ denotes addition modulo 2, $|x\rangle$ is an n-qubit register and $|y\rangle$ one qubit. By setting $|y\rangle = |0\rangle$, we have

$$U_f|x, 0\rangle \longrightarrow |x, f(x)\rangle. \tag{1.43}$$

Between the most useful and frequent quantum computing techniques belongs the Walsh-Hadamard transform (WHT) shown in Figure 1.5. It consist of Hadamard gates performed on n qubits initialized in $|0\rangle$ states. It is in fact an *efficient* transform that uses n quantum gates to create a homogenous superposition of all 2^n computational basis states.

Performing the WHT on the first n qubits followed by the action of U_f, we have

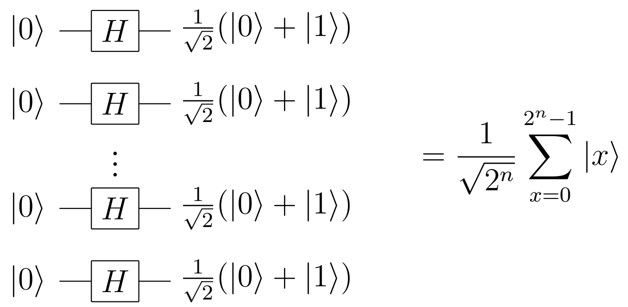
$|0\rangle$
H
$\frac{1}{\sqrt{2}}(|0\rangle + |1\rangle)$
$= \frac{1}{\sqrt{2^n}} \sum_{x=0}^{2^n-1} |x\rangle$

Figure 1.5: The Walsh-Hadamard transform. $|x\rangle$ denotes an n-qubit basis state that corresponds to the binary representation of x: $|x\rangle = |x_n \dots x_1\rangle$, $x_i \in \{0,1\}$, $x = \sum_{i=1}^{n} x_i \cdot 2^{i-1}$.

$$\underbrace{|0\rangle \otimes \ldots \otimes |0\rangle}_{n \text{ qubits}} \otimes |0\rangle \xrightarrow{\text{WHT}} \frac{1}{\sqrt{2^n}} \sum_x |x, 0\rangle \xrightarrow{U_f} \frac{1}{\sqrt{2^n}} \sum_x |x, f(x)\rangle. \tag{1.44}$$

As can be seen in (1.44), one action of U_f evaluates $f(x)$ for all x simultaneously. However, this parallelism itself is not very useful, because one measurement can reveal only one $f(x)$. *Efficient* quantum algorithms in addition require some methods of extracting the information from such superposition states, for example by the quantum Fourier transform (see Section 2.1).

1.4 Quantum computational complexity

Quantum computers which differ substantially from classical computing devices also bring new complexity classes. Before we start with their brief discussion, we will review few of the most important classical ones, namely **P**, **NP**, and **BPP**.

Suppose a problem is specified by giving n bits as input. We adopt the usual chief distinction between problems that can be solved using resources which are bounded by a *polynomial* in n and problems that require resources that grow faster than any polynomial. Such problems are usually denoted as *exponentially*[3] scaling.

Decision problems which can be solved in polynomial time on a classical computer[4] belong to the **P** (*polynomial*) complexity class. These problems are considered as tractable. On the contrary, without stating anything about time needed for solving a problem, decision problems whose ”yes” instances can be easily (in polynomial time) verified when given an appropriate solution (“witness”) belong to the **NP** (*nondeterministic polynomial*) class. Problems which are in **NP** and not known to be in **P** are considered as hard. The „hardest“ problems in **NP** in the sense that solving them in time t allows any other problem in **NP** to be solved in time $\mathcal{O}(\text{poly}(t))$ are so-called **NP**-complete. The most famous open problem in computer science is whether or not there are problems in **NP** which are not in **P**, abbreviated as $\mathbf{P} \overset{?}{=} \mathbf{NP}$. In other (simpler) words, it asks whether every problem whose solution can be quickly verified by a classical computer can also be quickly solved on it.

---

[3] Despite a function describing the growth of required resources need not to be a true exponential.

[4] More precisely on a deterministic Turing machine [28].

The **BPP** (*bounded-error probabilistic polynomial*) class contains decision problems solvable by a classical computer[5] in polynomial time, with an error probability of at most 1/3 for all instances. This error probability can be easily suppressed by a few repetitions of an algorithm, because it decreases exponentially with a number of repetitions. For this reason, **BPP** even more than **P** is usually considered as a class of decision problems that are *efficiently* solvable on a classical computer.

Because the nature of quantum mechanics is probabilistic (we always measure different states with certain probabilities), its evident that quantum computational complexity classes will be analogues of classical probabilistic ones. The **BQP** (*bounded-error quantum polynomial*) class is a quantum analogue of **BPP**. It contains all decision problems that can be solved with bounded probability of error using a polynomial size quantum circuit. Because quantum computers are essentially at least as powerful as classical ones (they can *efficiently* simulate classical computers [28]), **BQP** contains **P** and **BPP** ($\mathbf{P} \subseteq \mathbf{BPP} \subseteq \mathbf{BQP}$). On the other hand, despite being able to perform tasks like integer factorization *efficiently* [7, 8], it is believed that quantum computers are not capable of solving *all* **NP** problems *efficiently*, i.e. to solve any **NP**-complete problem *efficiently*.

The quantum analogue of **NP** is called **QMA** (*Quantum Merlin Arthur*). It contains decision problems that can be verified by a quantum computer in a polynomial time. **QMA** (like **NP**) covers many problems that are important to physics and chemistry. For example the ground state problem of a *general* two-body local Hamiltonian was recently proved to be **QMA**-complete [34], therefore hard even for a quantum computer. However, Hamiltonians typically occurring in chemical physics possess special symmetry and structure, which allows us to find a good enough approximate solution in a polynomial time by methods of quantum chemistry on a classical computer or by so called adiabatic state preparation [12] on a quantum computer. This approximate solution can then be employed as an initial guess and the problem becomes exactly solvable in a polynomial time on a quantum computer. The way how this is done is discussed in detail in Chapter 3.

---

[5] More precisely by a *probabilistic* Turing machine [28].

1.5 Physical realization of quantum computers

Quantum computing as a purely mathematical computational model is fascinating and it indeed brought new insights into math and theoretical physics, but its physical realization is of course the ultimate goal. However, experimental realization of quantum circuits and algorithms has proven extremely challenging. On one hand, a quantum computing device must be very well isolated from the rest of the Universe not to undergo an environmental quantum information leakage through the process known as decoherence [35]. On the other hand, the operation of a quantum computer must be under programmer's control, i.e. affected from the outside in a well defined manner. Although these demands are somewhat contradictory, they can be fulfilled, as has been demonstrated by many proof-of-principle experiments with different types of quantum technologies [28, 36, 37]. Many research groups around the world are working towards the highly ambitious technological goal of building a quantum computer being able to dramatically improve computational power for particular tasks.

The general requirements for the implementation of quantum computation [38, 37] can be summarized as follows:

1. Scalability: the computer must operate in a Hilbert space whose dimension can grow exponentially without an exponential cost in resources (such as time, space or energy). We may achieve this by adding "well-characterized" qubits to our system.

2. Ability to initialize the state of the qubits to a simple fiducial state, such as $|000\ldots\rangle$, from which the computation begins.

3. Fault tolerance: as was already broached, quantum information is very fragile. In contrast to conventional computers, quantum computers will be very susceptible to noise. The main sources of noise are the decoherence [35], which is due to incomplete isolation of the quantum system from its environment and control errors, which are caused by calibration errors and random fluctuations in control parameters. No system is completely free of noise, but small amounts may be removed through various techniques gathered under the name of "quantum error correction" (QEC) [33]. The truly remarkable result that arises from the fault-tolerant circuit design and ability to perform dynamical error correction is the threshold theorem [33]. It in fact says that if the noise is below some threshold, an arbitrarily long quantum computation can be realized. The critical value of a threshold depends on the computer hardware, the sources of error, and the protocols used for QEC.

4. Universal logic: the large Hilbert space must be accessible using a finite set of control operations. In Section 1.2.3, we have already dealt with the universal sets of quantum

gates for the quantum circuit model.

5. Ability to measure the output result.

We will very briefly discuss three quantum technologies that belong to the current leading ones and have been used recently for the first proof-of-principle experiments relevant to quantum chemistry [20, 21, 23, 22, 39], namely optical quantum computing, nuclear magnetic resonance (NMR) quantum computing, and quantum computing employing trapped ions.

Optical quantum computers

When photons carry the quantum information, we speak about optical quantum computers [40]. In this case, qubit can be realized e.g. as the polarization state of a photon, but alternative encodings on the basis of location ("dual-rail" representation) or timing are also possible. Single qubit gates (polarization rotations) can in the former case be easily realized using waveplates made of birefringent material. The biggest difficulty of this approach is to achieve the interactions between photons which are needed for two-qubit gates. In fact, the necessary interactions appear to require optical nonlinearities stronger than those available in conventional nonlinear media.

In 2001, Knill, Laflamme and Milburn (KLM) showed that scalable quantum computing is possible using only single-photon sources and detectors, and linear optical circuits [41]. This original scheme, however, is non-deterministic and to realize a near-deterministic CNOT gate, really huge resource overhead is required. Employing the ideas of the cluster state quantum computing [42] allowed to reduce this resources by 3-4 orders of magnitude, making an all-optical approach far more attractive [40]. Another promising step towards a large scale optical quantum computing are chip-scale waveguide quantum circuits [43, 44].

Recently, Lanyon et al. presented the first proof-of-principle experimental realization of the quantum FCI (see Chapter 3) computation of the hydrogen molecule in a minimal basis employing the optical quantum computer [20].

NMR quantum computers

Another quantum computing technology that has been studied extensively since its proposal in 1997 [45, 46] is a liquid-state NMR, a technique very well known to chemists. In this case, nuclear spins serve as the carriers of the quantum information. Different nuclear spins in a strong magnetic field can be identified through their Larmour frequency [47]. The NMR spectroscopy relies on the fact that Larmour frequencies corresponding to chemically inequivalent atoms in a molecule varies due to the shielding effect of surrounding electrons.

Single qubit gates can be realized as selective resonant radio-frequency pulses and two-qubit interactions arise from the indirect coupling mediated through electrons in chemical bonds (direct dipole-dipole interactions are averaged away due to a rapid molecular motion in a solution). These interactions as well as interactions of individual spins with a static magnetic field are always present in a system Hamiltonian. Nevertheless, they can be effectively turned off by refocusing techniques [28] (so called no-operation gate). Measurement is achieved by observing the induced current in a coil surrounding the sample of an *ensemble* of such qubits. It is not a projective measurement, but rather a weak *ensemble* measurement which monitors the state of the spin system without changing it [48].

An important challenge for NMR quantum computers is the initialization step. Due to a very small energy gap between α and β spin states ($\hbar\omega \ll k_{\mathrm{B}}T$), the system is in a high entropy mixed state at room temperature. The first proposals employed pseudo-pure-state techniques (temporal, spacial, and logical labeling methods) [28], which isolate the signal of an initialized pure states against a high-entropy background, but are not scalable. A promising alternative is the algorithmic cooling [48], especially in connection with the solid-state NMR which has the potential for much higher initial nuclear polarizations [49].

NMR is at the moment probably the simplest technology for building few-qubit demonstration devices. Experiments with up to impressive twelve qubits have been realized [50]. Among others, Du et al. [21] recently implemented the similar quantum FCI computation of the hydrogen molecule as in [20], but with adiabatically prepared initial states. Also the first proof-of-principle experiment simulating the chemical reaction dynamics, namely the izomerization of substituted malonaldehydes, has been performed on the three-qubit NMR quantum computer [23]. Very recently, Li et al. [22] presented the three-qubit NMR experiment solving the ground state problem of the Heisenberg spin model.

Trapped ions quantum computers

Atomic ions that can be confined in free space with nanometer precision by electromagnetic fields represent another promising approach to quantum computing devices. Their certain energy levels form very reliable qubits with long coherence times (typically in the range of seconds and longer).

Initial state preparation is realized by cooling the system of trapped ions down into their collective motional ground state (as well as hyperfine ground states of individual ions). Single qubit gates are carried out by means of Rabi flopping, i.e. coherent transitions between the internal states of ions, which are performed by applying a resonant laser pulse for a fixed time. Two qubits can be entangled through a laser-induced coupling of internal states of ions mediated by the lowest collective vibrational mode, the centre-of-mass motion [51]. Measurements with almost 100 % efficiency are carried out by the state-dependent optical fluorescence detection.

One of the promising steps towards a large scale trapped-ion quantum computer which avoids problems with large number of ions participating in the collective motion were presented by Home et al. [52]. In this case, individual ions are shuttled between various zones of a complex trap structure by controlled electrical forces and entangling gates need only operate with a small number of ions. Very recently, Lanyon et al. [39] presented a trapped-ion realization of a digital quantum simulation of six interacting spins with sequences of up to 100 gates.

There exist a large number of other approaches to quantum computing devices that haven't been mentioned here, e.g. trapped neutral atoms, optical cavity quantum electrodynamics, superconducting qubits, and many others. As is usual, each of them possesses some advantages, but also some drawbacks. Indeed, the time will show whether one of the presently known quantum technologies will be able to achieve the ambitious goal of a large-scale quantum computer or some presently unknown one will be discovered.

2 Quantum algorithms

In this chapter, we deal with *efficient* quantum algorithms that are important for the quantum full configuration interaction method presented in Chapter 3, most importantly the quantum Fourier transform and the phase estimation algorithm.

2.1 Quantum Fourier transform

The classical discrete Fourier transform takes as an input a vector of complex numbers $(x_0, \ldots, x_{N-1})$ and outputs the elements of another vector $(y_0, \ldots, y_{N-1})$ according to the equation

$$y_k = \frac{1}{\sqrt{N}} \sum_{j=0}^{N-1} x_j e^{2\pi ijk/N}. \tag{2.1}$$

Similarly, the quantum Fourier transform (QFT) operates on an orthonormal basis of n qubits: $|0\rangle \ldots |2^n - 1\rangle$ and is defined as an operator $\hat{U}_{\mathrm{QFT}}$

$$\hat{U}_{\mathrm{QFT}} |k\rangle = \frac{1}{\sqrt{N}} \sum_{j=0}^{N-1} e^{2\pi ijk/N} |j\rangle, \qquad N = 2^n, \tag{2.2}$$

where the kets are numbered by a binary representation of integers (like in Figure 1.5). Equivalently, the action on an arbitrary state can be written

$$\hat{U}_{\mathrm{QFT}} \left(\sum_{j=0}^{N-1} x_j |j\rangle \right) = \sum_{k=0}^{N-1} y_k |k\rangle, \tag{2.3}$$

where the amplitudes y_k are the discrete Fourier transform of the amplitudes x_j. It can be shown [28] that $\hat{U}_{\mathrm{QFT}}$ is a unitary operator.

As will be shown bellow, the QFT can be performed with just $\mathcal{O}(n^2)$ operations (quantum gates). This is in sharp contrast to the classical fast Fourier transform (FFT) with the scaling $\mathcal{O}(N \log_2 N = n2^n)$. The quantum version thus achieves an *exponential* speedup over its classical counterpart.

We may rewrite the action of the QFT on $|j\rangle$ in the following way [28]

$$\begin{aligned}
|j\rangle &\rightarrow \frac{1}{\sqrt{2^n}}\sum_{k=0}^{2^n-1} e^{2\pi i jk/2^n}|k\rangle && (2.4)\\
&= \frac{1}{\sqrt{2^n}}\sum_{k_1=0}^{1}\dots\sum_{k_n=0}^{1} e^{2\pi i j(\sum_{l=1}^{n} k_l 2^{l-1-n})}|k_n\dots k_1\rangle && (2.5)\\
&= \frac{1}{\sqrt{2^n}}\sum_{k_1=0}^{1}\dots\sum_{k_n=0}^{1}\bigotimes_{l=n}^{1} e^{2\pi i j k_l 2^{l-1-n}}|k_l\rangle && (2.6)\\
&= \frac{1}{\sqrt{2^n}}\bigotimes_{l=n}^{1}\left[\sum_{k_l=0}^{1} e^{2\pi i j k_l 2^{l-1-n}}|k_l\rangle\right] && (2.7)\\
&= \frac{1}{\sqrt{2^n}}\bigotimes_{l=n}^{1}\left[|0\rangle + e^{2\pi i j 2^{l-1-n}}|1\rangle\right] && (2.8)\\
&= \frac{\Big(|0\rangle + e^{2\pi i 0.j_1}|1\rangle\Big)\Big(|0\rangle + e^{2\pi i 0.j_2 j_1}|1\rangle\Big)\dots\Big(|0\rangle + e^{2\pi i 0.j_n\dots j_1}|1\rangle\Big)}{\sqrt{2^n}}, && (2.9)
\end{aligned}$$

where $0.j_n\dots j_1$ denotes the binary fraction

$$\frac{j_n}{2} + \frac{j_{n-1}}{4} + \dots + \frac{j_1}{2^n}.$$

The *efficient* quantum circuit for the QFT, which is shown in Figure 2.1, can be easily derived from the product state representation (2.9). R_j gates[1] are represented by the following matrices

$$R_j = \begin{pmatrix} 1 & 0 \\ 0 & e^{2\pi i/2^j} \end{pmatrix}. \tag{2.10}$$

Let's now examine the QFT circuit in detail. Since $e^{2\pi i 0.j_n} = -1$ when $j_n = 1$, and is +1 when $j_n = 0$, the first Hadamard gate in fact produces

$$\frac{1}{\sqrt{2}}\Big(|0\rangle + e^{2\pi i 0.j_n}|1\rangle\Big)|j_{n-1}\dots j_1\rangle, \tag{2.11}$$

Subsequent controlled-R_2 rotation creates

$$\frac{1}{\sqrt{2}}\Big(|0\rangle + e^{2\pi i 0.j_n j_{n-1}}|1\rangle\Big)|j_{n-1}\dots j_1\rangle. \tag{2.12}$$

Analogously, each of the controlled rotations $R_3\dots R_n$ adds an extra bit to the phase of the coefficient of the first $|1\rangle$, leading to the state

---

[1] Up to a global phase, they correspond to $R_z(2\pi/2^j)$ rotations (1.17).

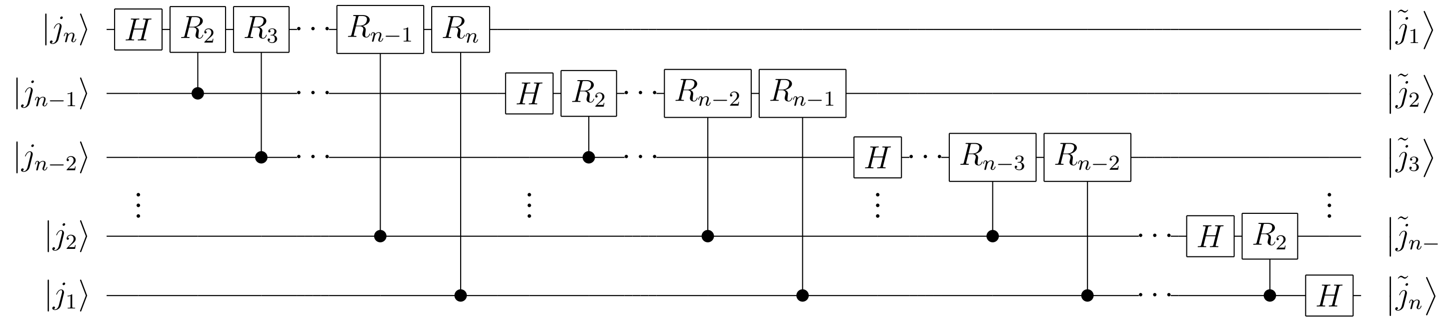

Figure 2.1: The quantum Fourier transform circuit, where by $\left|\tilde{j}_1\right\rangle$ we denote the state $|0\rangle + e^{2\pi i 0.j_n \ldots j_1}|1\rangle$, … up to $\left|\tilde{j}_n\right\rangle = |0\rangle + e^{2\pi i 0.j_1}|1\rangle$. Note that qubits of the result are in a reversed order.

$$\frac{1}{\sqrt{2}}\Big(|0\rangle + e^{2\pi i 0.j_n j_{n-1}\ldots j_1}|1\rangle\Big)|j_{n-1}\ldots j_1\rangle. \tag{2.13}$$

Similar procedure on the remaining qubits gives a final state

$$\frac{1}{\sqrt{2^n}}\Big(|0\rangle + e^{2\pi i 0.j_n \ldots j_1}|1\rangle\Big)\Big(|0\rangle + e^{2\pi i 0.j_{n-1}\ldots j_1}|1\rangle\Big)\ldots\Big(|0\rangle + e^{2\pi i 0.j_1}|1\rangle\Big). \tag{2.14}$$

When comparing Eq. 2.14 with Eq. 2.9, we can see that the circuit from Figure 2.1 performs the QFT, the only difference is that qubits are in a reversed order after its application. This is usually not a problem in a real physical implementation, but one must count with it or, alternatively, if necessary, the qubits can be swapped with SWAP gates [2]. One SWAP gate can be realized with three CNOTs, as is shown in Figure 2.2.

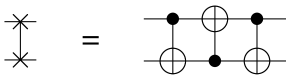

Figure 2.2: The SWAP gate by means of three CNOT gates.

It should be noted that even though the QFT can be done *exponentially* faster than the FFT, it cannot be used as an efficient *straightforward replacement* of the Fourier transform itself. It would indeed require to prepare an arbitrary state of n qubits and also measure all of the complex amplitudes at the end, which cannot be done *efficiently*. Nevertheless the QFT is a key part of the phase estimation algorithm [28] (contained also in the Shor's factoring algorithm [7, 8]) as will be shown in Section 2.3.

---

[2] At most $n/2$ SWAP gates are necessary.

$$\text{controlled-}R_j = \begin{pmatrix} 1 & 0 & 0 & 0 \\ 0 & 1 & 0 & 0 \\ 0 & 0 & 1 & 0 \\ 0 & 0 & 0 & e^{2\pi i/2^j} \end{pmatrix} \dots |11\rangle \quad \Rightarrow$$

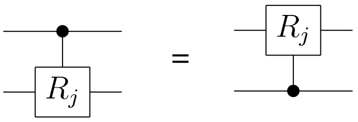

Figure 2.3: Matrix representation of the controlled-R_j gate.

2.2 Semiclassical approach to quantum Fourier transform

The QFT circuit can in fact be greatly simplified using the semiclassical (measurement based) approach [53], since the controlled-R_j gates (cf. Figure 2.3) are diagonal matrices with the only non-unit element on a diagonal that corresponds to the $|11\rangle$ basis state. The roles of control and target qubits thus can be interchanged, leading to an alternative QFT circuit shown in Figure 2.4.

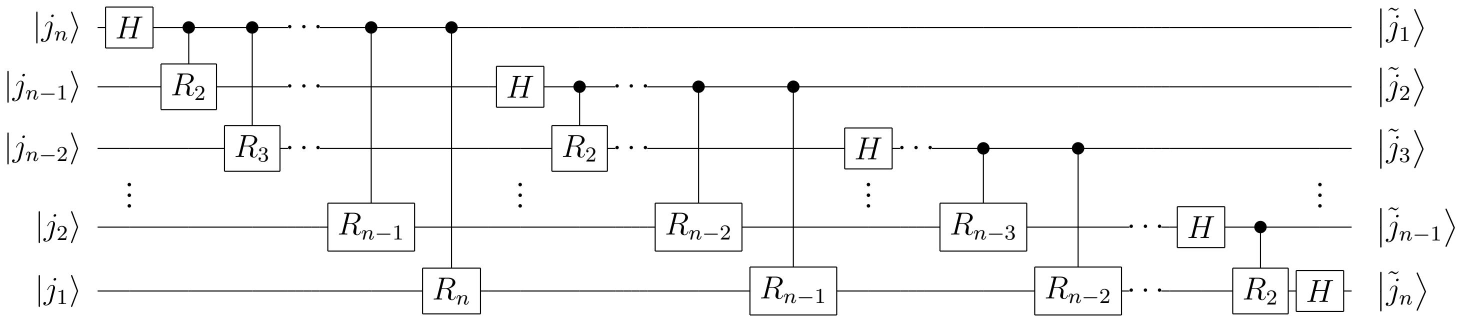

Figure 2.4: An alternative QFT circuit suitable for semiclassical simplifications.

Notice that in this circuit gates acting on each qubit [except the first (top most) and the last ones where the corresponding parts are missing] obey the general structure: first, R_j gates controlled by previous qubits are applied, then the Hadamard gate is applied, and finally they serve as control qubits for the subsequent ones. Since the state of each qubit does not change after the application of the Hadamard gate, when the measurement follows after the QFT, it can be performed immediately after this gate. Rather than employing controlled R_j gates, one can apply only the corresponding one qubit gates depending on the results of individual measurements. Moreover, all R_j gates acting on a kth qubit can be merged into a single rotation gate[3]

---

[3] We adopt the usual notation and denote this rotation gate as R_z, however it must be noted that it differs from the conventional R_z gate defined in Eq. 1.17 by a global phase factor.

$$R_z(\omega_k) = \begin{pmatrix} 1 & 0 \\ 0 & e^{2\pi i \omega_k} \end{pmatrix}, \tag{2.15}$$

whose angle ω_k depends on the results of previously measured qubits (q_i) according to the formula

$$\omega_k = \sum_{i=2}^{n-k+1} \frac{q_{k+i-1}}{2^i}, \qquad k:\ n \longrightarrow 1. \tag{2.16}$$

Figure 2.5 shows the semiclassical QFT circuit pattern which is the same for all qubits. The big advantage of the aforementioned approach is that we have actually replaced two-qubit gates by single qubit ones (controlled by a classical signal). This technique is especially useful in connection with the phase estimation algorithm where it leads to the formulation of its iterative version (IPEA, Section 2.4).

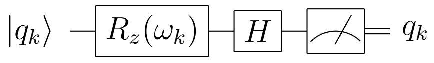

Figure 2.5: Simplified, measurement based circuit for the kth qubit of the QFT.

2.3 Phase estimation algorithm

The phase estimation algorithm (PEA) [28] is a quantum algorithm for obtaining an eigenvalue of a unitary operator $\hat{U}$, based on a given initial guess of the corresponding eigenvector. Since a unitary $\hat{U}$ can be written as $\hat{U} = e^{i\hat{H}}$, with $\hat{H}$ Hermitian, the PEA can be viewed as a quantum substitute of the classical diagonalization.

Suppose that $|u\rangle$ is an eigenvector of $\hat{U}$ and that it holds

$$\hat{U}|u\rangle = e^{2\pi i\phi}|u\rangle, \qquad \phi \in \langle 0, 1), \tag{2.17}$$

where ϕ is the phase which is estimated by the algorithm. Quantum register is divided into two parts. The first one, called the read-out part, is composed of m qubits on which the binary representation of ϕ is measured at the end and which is initialized to the state $|0\rangle^{\otimes m}$. The second part contains the corresponding eigenvector $|u\rangle$.

The PEA quantum circuit is shown in Figure 2.6. The application of Hadamard gates on all qubits (the Walsh-Hadamard transform, see Figure 1.5) in the first part of the register gives

$$|\mathrm{reg}\rangle = \frac{1}{\sqrt{2^m}}\Big(|0\rangle + |1\rangle\Big) \ldots \Big(|0\rangle + |1\rangle\Big)|u\rangle = \frac{1}{\sqrt{2^m}} \sum_{j=0}^{2^m-1} |j\rangle|u\rangle. \tag{2.18}$$

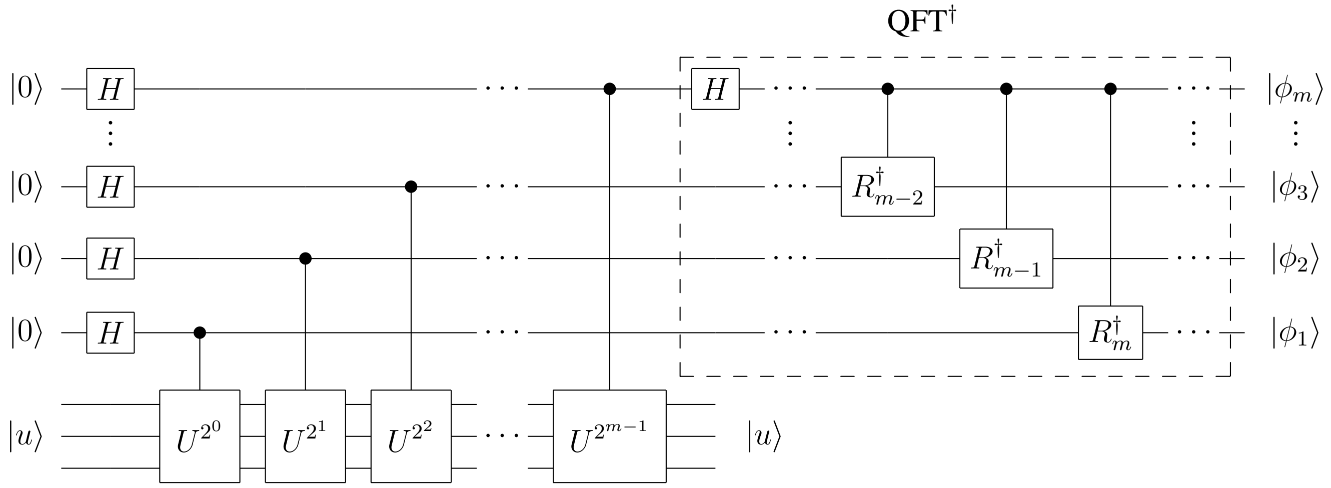

Figure 2.6: The PEA circuit with the highlighted part corresponding to the inverse QFT.

Next, after the application of a sequence of controlled powers of $\hat{U}$, the register is transformed into

$$\begin{aligned} |\text{reg}\rangle &= \frac{1}{\sqrt{2^m}}\Big(|0\rangle + e^{2\pi i 2^{m-1}\phi}|1\rangle\Big)\Big(|0\rangle + e^{2\pi i 2^{m-2}\phi}|1\rangle\Big)\ldots\Big(|0\rangle + e^{2\pi i 2^{0}\phi}|1\rangle\Big)|u\rangle = \\ &= \frac{1}{\sqrt{2^m}}\sum_{j=0}^{2^m-1} e^{2\pi i j\phi}|j\rangle|u\rangle. \end{aligned} \tag{2.19}$$

The crucial part of the PEA is the *efficient* inverse quantum Fourier transform (QFT†, highlighted in Figure 2.6) performed on the read-out part of the register. If the phase can be expressed exactly with m bits

$$\phi = 0.\phi_1\phi_2\ldots\phi_m = \frac{\phi_1}{2} + \frac{\phi_2}{2^2} + \ldots + \frac{\phi_m}{2^m}, \qquad \phi_i \in \{0,1\}, \tag{2.20}$$

it (and consequently the eigenvalue) is recovered with unity probability by a measurement on the first part of the quantum register, which is by the QFT† transformed into $|2^m\phi\rangle$.

The situation is more complicated when ϕ cannot be expressed exactly with m bits. Then we can write

$$\phi = \tilde{\phi} + \delta 2^{-m}, \tag{2.21}$$

where $\tilde{\phi} = \phi_1\phi_2\ldots\phi_m$ denotes the first m bits of the binary expansion and $\delta\,:\; 0 \le \delta < 1$ is a remainder. The closest m-bit estimators of ϕ correspond to either $\tilde{\phi}$ (rounding down) or $\tilde{\phi} + 2^{-m}$ (rounding up). When we label the probabilities of measuring these two estimators by P_{down} and P_{up}, it can be shown (e.g. [54]) that the sum $P_{\text{down}} + P_{\text{up}}$ decreases monotonically

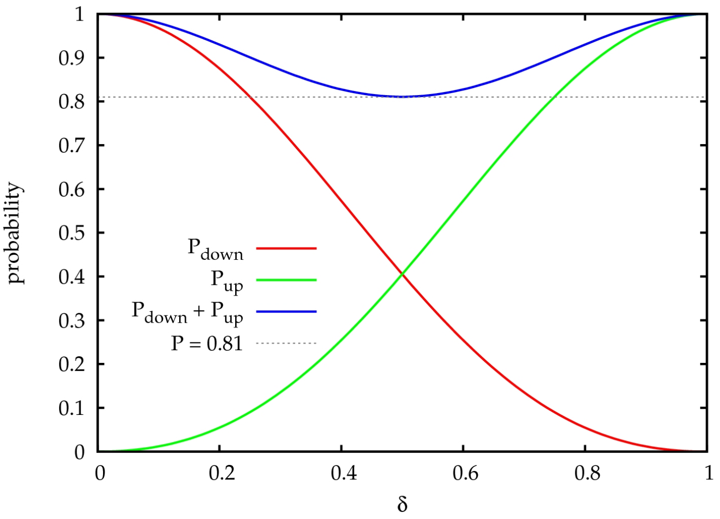

Figure 2.7: The dependence of success probabilities of the PEA on δ for $m = 20$. P_{down} and P_{up} denote the success probabilities corresponding to rounding the exact phase up/down to m binary digits.

with increasing m. The explicit forms of P_{down} and P_{up} can be found in Appendix A. The dependence of P_{down} and P_{up} on δ for $m = 20$ is presented in Figure 2.7. In the limit $m \to \infty$, the lower bound reads [54]

$$P_{\text{down}}(\delta = 1/2) + P_{\text{up}}(\delta = 1/2) = \frac{4}{\pi^2} + \frac{4}{\pi^2} > 0.81. \tag{2.22}$$

For further details on probability analysis of the PEA, we refer the reader to Appendix A.

If the desired eigenvector is not known explicitly (as is typically the case in quantum chemistry), we can start the algorithm with an arbitrary initial guess vector $|\psi\rangle$, which can be expanded in terms of eigenvectors of $\hat{U}$

$$|\psi\rangle = \sum_i c_i |u_i\rangle. \tag{2.23}$$

The probability of obtaining the *exact* m-bit ϕ_i is due to linearity of the algorithm $|c_i|^2$. It is important to note that the initial guess does not influence the accuracy of the phase, only the probability with which the phase of a particular eigenstate is measured. When ϕ_i cannot be expressed with m bits, the lower bound for $P_{\text{down}} + P_{\text{up}}$ corresponding to ϕ_i is equal to $0.81 \cdot |c_i|^2$.

For concreteness, we give a simple demonstrative example of the phase estimation procedure. Let $\hat{U}$ have the following matrix form

$$U = \begin{pmatrix} -1 & 0 \\ 0 & i \end{pmatrix}, \tag{2.24}$$

with eigenvalues and eigenvectors presented in Table 2.1. Two qubits in the read-out part of the register are sufficient for both phases. The PEA circuit with the second part of the register initialized to the $|u_2\rangle$ state, which recovers the phase corresponding to the second eigenvalue, is shown in Figure 2.8.

#	eigenvalue	eigenvector	phase (ϕ)	binary representation of ϕ
1	$-1 = e^{i\pi}$	$\lvert u_1\rangle = (1,0)^T = \lvert 0\rangle$	0.5	$0.\phi_1\phi_2 = 0.10$
2	$i = e^{i\pi/2}$	$\lvert u_2\rangle = (0,1)^T = \lvert 1\rangle$	0.25	$0.\phi_1\phi_2 = 0.01$

Table 2.1: Eigenvalues, eigenvectors and corresponding phases of U (2.24).

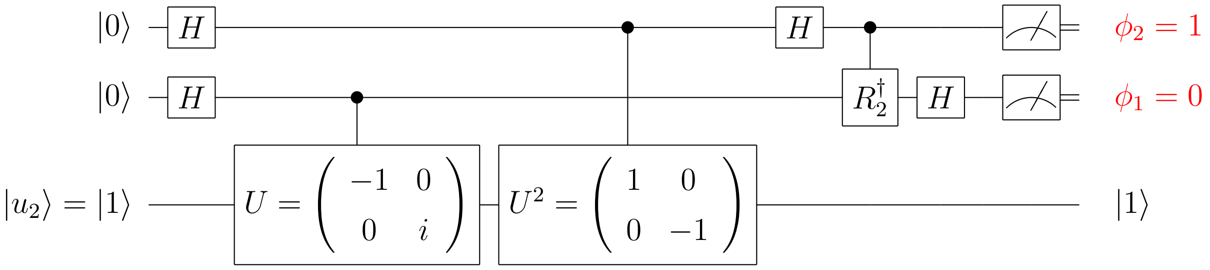
$|0\rangle$
$|0\rangle$
$|u_2\rangle = |1\rangle$
H
H
$U = \begin{pmatrix} -1 & 0 \\ 0 & i \end{pmatrix}$
$U^2 = \begin{pmatrix} 1 & 0 \\ 0 & -1 \end{pmatrix}$
H
$R_2^\dagger$
H
$\phi_2 = 1$
$\phi_1 = 0$
$|1\rangle$

Figure 2.8: Example of the PEA circuit which recovers the second phase (see Table 2.1) of U (2.24) with unity probability.

The PEA, as an *efficient* quantum diagonalization method, is a key part of the quantum full configuration interaction method (Chapter 3). As was already mentioned, it is also contained in probably the most famous known quantum algorithm, namely the Shor's algorithm for integer factorization [7, 8].

2.4 Iterative phase estimation algorithm

Using the semiclassical QFT [53] (Section 2.2), the PEA circuit can be simplified, having only one ancillary qubit in the read-out part of the quantum register. The algorithm then proceeds in an iterative manner [iterative phase estimation algorithm (IPEA)]. The k-th iteration of this scheme is presented in Figure 2.9. Note that as the PEA uses the inverse QFT, the angle ω_k (2.16) must be negative now. The algorithm is iterated backward from the least significant bits of ϕ to the most significant ones, i.e. for k going from m to 1. For our purposes, the presented IPEA, which is the *unitary* matrix eigenvalue algorithm, is completely adequate, but we would like to note that Wang et al. recently presented a modified version of the IPEA capable of finding eigenvalues of *non-unitary* matrices [55].

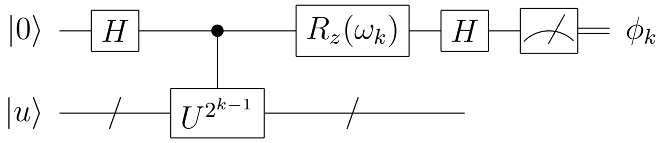

Figure 2.9: The k-th iteration of the IPEA. The feedback angle depends on the previously measured bits, k is iterated backwards from m to 1.

The IPEA is in fact completely equivalent to the original (multi-qubit) PEA [54]. It exhibits the same behaviour - decreasing of the success probability when the phase cannot be expressed exactly in a particular number of bits. One possibility of a success probability amplification is performing more iteration steps (more than is the desired accuracy of ϕ): when extracting $m' = m + \log(2 + 1/2\epsilon)$ bits, the phase is accurate to m binary digits with probability at least $1 - \epsilon$ [28]. This method is however not very useful, since implementing $\hat{U}^{2^{k-1}}$ for large k is the algorithm's bottleneck in a realistic noisy environment [56].

Another alternative [56] is to repeat the measurement for the least important bits of the phase binary expansion. Using the majority voting (for bit value 0 or 1), the effective error probability decreases exponentially with the number of repetitions according to the binomial distribution. This measurement repetition only for the few least important bits of ϕ is unfortunately possible only if the exact eigenstates of $\hat{U}$ are available.

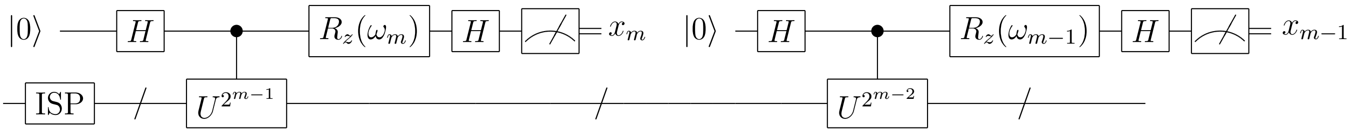

a) Maintaining the second part of the quantum register during all iterations (version **A**).

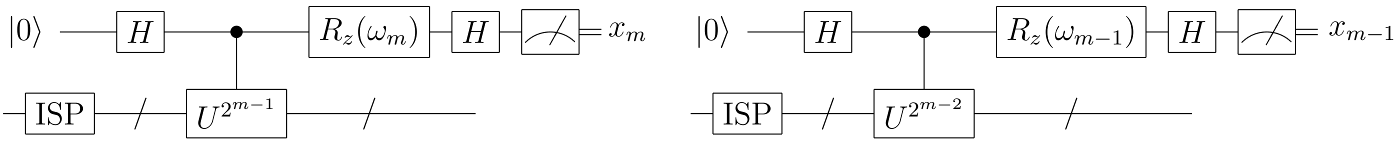

b) Repeated initial state preparation in each iteration (version **B**).

Figure 2.10: Comparison of the two versions of IPEA, $\boxed{\text{ISP}}$ denotes the initial state preparation.

When working with general initial states (as in a practical application to quantum chemistry), two scenarios are possible [24], as shown in Figure 2.10. Maintaining the second part of the quantum register during all iterations and amplification of the success probabilities by repeating the whole process number of times is the first possibility. This version was denoted as **A** version of IPEA. The biggest advantage of this approach is that one always ends up with one of the eigenstates of $\hat{U}$ in the second part of the quantum register as was also the case of the PEA. It happens through successive collapses of the system state into the corresponding eigensubspace and is demonstrated on the hydrogen molecule with random initial states in Figure 2.11. The biggest disadvantage that complicates the potential physical realization of this scheme is the requirement for a long coherence time of the quantum register. We would like to note here that when amplifying the success probability by repeating the whole process, it must be higher than 0.5 to be sure that we get the energy of the right state. This, however, is not necessary for the ground state energy which can always be identified by the lowest eigenvalue [24, 22].

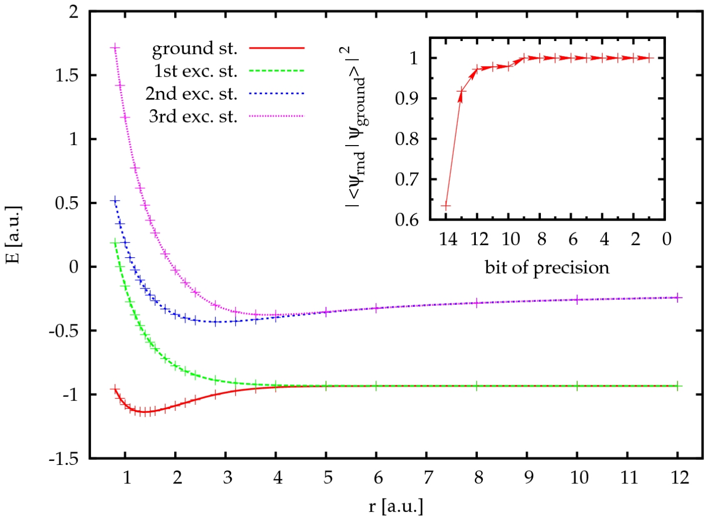

Figure 2.11: Energies of the four electronic states of H_2 in STO-3G basis which were obtained by the qFCI method (IPEA version **A**) with randomly generated initial guess states. Small figure inside presents the increasing overlap between the actual state of the second part of the quantum register and the exact wave function for one of random runs of the algorithm leading to the ground state.

Another possibility is to initialize the second part of the quantum register at every iteration step (**B** version of IPEA). Every iteration step (not only the least important bits of ϕ as in [56]) must be repeated and measurement statistics performed. One could otherwise possibly mix bits belonging to different eigenvalues in different iterations and obtain an unphysical result.

The biggest advantage of this approach is avoidance of the long coherence times and therefore potentially easier physical implementation. On the other hand, the biggest disadvantage is that no improving of the overlap between the actual state of the quantum register and the exact wave function occurs during the iterations and one must “fight” the overlap problem at every iteration step. But as will be shown in Chapter 4 on the example of the methylene molecule [24], small number of repetitions of each iteration is sufficient for amplification of the success probability almost to unity, when a suitable initial state of the quantum register is used.

At the end of this section, we would like to mention a different way of reducing the number of read-out qubits required by the PEA, which was suggested in the seminal work by Aspuru-Guzik et al. [12]. Their recursive variant of the PEA uses four qubits in the read-out part of the quantum register on which the phase (and therefore also the energy) is successively improved. It starts with measuring the first four bits of the phase ϕ. The Hamiltonian is then shifted by this reference value and a four-bit estimate of the deviation of the phase from the reference one on the half of the interval computed. The procedure is iteratively repeated and the overall effect is a gain of one additional bit of ϕ at each iteration step (thus the same as in the IPEA). In spite of the fact that this method uses four read-out qubits instead of one which is used by the IPEA, it is worth mentioning. First of all, it was the first iterative version of the PEA applied to the Hamiltonian eigenvalue problem [12]. Secondly, it recovers the energy starting from the most important bits towards the least important ones (in contrast to the IPEA), which can be advantageous in certain situations.

3 Quantum full configuration interaction method

The PEA/IPEA can be used for efficient computations of eigenvalues of *local* Hamiltonians [10]. If we take $\hat{U}$ in the form

$$\hat{U} = e^{i\tau\hat{H}}, \tag{3.1}$$

where $\hat{H}$ is a local Hamiltonian and τ a suitable parameter assuring ϕ being in the interval $\langle 0, 1)$, then the algorithm reveals the energy spectrum of $\hat{H}$. The whole procedure can be simply viewed as a time propagation of a trial wave function followed by the QFT switching from the time to energy domain and a measurement projecting out a certain eigenstate.

In this chapter, we discuss the application to non-relativistic molecular Born-Oppenheimer electronic Hamiltonians. We will start with a mapping of quantum chemical wave functions onto a quantum register (Section 3.1). Section 3.2 briefly mentions the question of initial state preparation and Section 3.3 deals with the crucial part of the algorithm, namely the implementation of controlled powers of the exponential of molecular Hamiltonians (controlled "time propagation").

3.1 Mapping of quantum chemical wave functions onto quantum register

Several possible mappings of a quantum chemical wave function onto a register of qubits have been proposed. The simplest, but the least economical one in terms of the number of employed qubits, is so called direct mapping [12]. In this approach, individual spin orbitals are directly assigned to qubits, since each spin orbital can be either occupied or unoccupied, corresponding to $|1\rangle$ or $|0\rangle$ states. The inefficiency lies in the fact that it actually maps the whole Fock space of the system (states with different number of electrons) on the Hilbert space of the quantum register. For example, when working with wave functions built from Slater determinants containing two electrons in four spin orbitals with an additional restriction $M_S = 0$, only four determinants can contribute, but the computational basis consists of 16 states. The first one $|0000\rangle$ corresponds to the state with no electrons and the final one $|1111\rangle$ to the state with four of them. Relativistic generalization of this approach [25] assigns one qubit to one Kramers pair bispinor (A or B, analogy to α and β spin in non-relativistic treatment). The advantage of the direct mapping stems from the fact, that a general factorization scheme, i.e. an algorithm to systematically generate a quantum circuit implementing the exponential of the Hamiltonian is known (see Section 3.3.1).

Compact mappings from a subspace of fixed-electron-number wave functions, spin-adapted [12], or even symmetry-adapted wave functions employing the point group [13] or double group symmetry [25] to the register of qubits have also been proposed. However, *efficient* general factorization schemes are unfortunately not known for these mappings. The factorization to elementary quantum gates can be for small circuits performed either with numerical optimization techniques (e.g. with genetic algorithms [57]) or analytically [58, 59], but neither is *efficient*. Its use is motivated by the need to employ as few qubits as possible in today's experimental realizations [20, 21, 22] as well as simulations on classical computers.

3.2 Initial states for the algorithm

As the PEA/IPEA requires an initial state for the system part of the quantum register, the quantum full configuration interaction (qFCI) algorithm must be started with some initial guess of the corresponding eigenvector. For most Hamiltonians relevant in chemistry, obtaining such an initial guess is easy, but in general it can be a difficult problem, since the **QMA** complexity of the two-local Hamiltonian eigenvalue problem is hidden here. Generally, it holds that the closer is the initial guess to the exact wave function, the higher is the success probability of measuring the energy. As was shown in Refs. [17, 24] and will be discussed in Chapter 4, the simplest one-determinantal Hartree-Fock guess may not be successful in situations, where correlation (particularly the static one) plays an important role. In these situations, initial guess states from more sophisticated *polynomially* scaling methods can be used [e.g. complete active space self consistent field (CASSCF) method in a limited orbital CAS].

Besides determination of a suitable initial state, preparation can be a hard task as well, since such a vector can contain up to 2^n non-zero components in general and it cannot be performed *efficiently*. Fortunately, as will be shown in Chapter 4 on the example of methylene molecule, initial guesses including only few determinants in a superposition are sufficient for most purposes of quantum chemistry [24]. These states can be prepared e.g. with the procedure described by Ortiz et al. [4] which scales as $\mathcal{O}(N^2)$ in the number of determinants N.

Preparation of general molecular-like states from the combinatorial space of dimension $\binom{n}{m}$ corresponding to distributing m electrons among n spin orbitals was presented in [17]. Preparation of many-particle states in a superposition on a lattice which can be then propagated by quantum chemical dynamics algorithm [14] was studied in [16].

3.2.1 Adiabatic state preparation

A completely different approach to obtain the initial state is the adiabatic state preparation (ASP) method of Aspuru-Guzik et al. [12]. In the ASP method, one slowly varies the Hamiltonian of the quantum register, starting with a trivial one and the register in its (exactly known) ground state and ending with the final exact one in the following simple way

$$\hat{H} = (1-s)\hat{H}_{\text{init}} + s\hat{H}_{\text{exact}} \qquad s : 0 \longrightarrow 1. \tag{3.2}$$

If the change is slow enough (depending on the gap between the ground and the first excited state), the register remains in its ground state according to the adiabatic theorem [60]. Again, the **QMA** complexity manifests itself in the fact, that in the worst case the gap can become exponentially small with size of the problem. Fortunately for quantum chemistry, this seems not to be the case for a typical molecule.

In the compact mapping, $\hat{H}_{\text{init}}$ can be defined to have all matrix elements equal to zero, except H_{11}, which is equal to the (Dirac-)Hartree-Fock energy [12, 25].

Figure 3.1a demonstrates on the example of the SbH molecule the improvement of the IPEA (version **A**) ground state success probability during the ASP procedure. The dependence of the energy gap (ΔE) between the ground and the first excited state on the adiabatic transition parameter s is shown in Figure 3.1b. Although ΔE is getting close to 0 for $r = 8.0\ a_0$ and s going to 1, the ground state is becoming degenerate at this internuclear distance and this fact thus does not influence the IPEA success probability. We will discuss the relativistic qFCI method and its application to the SbH spin-orbit splitting in more detail in Chapter 5.

Recently, the ASP of the hydrogen molecule ground state has been realized experimentally on a NMR quantum simulator [21].

3.3 Controlled "time propagation"

To study the overall scaling of the qFCI algorithm, one must decompose the only multi qubit gate from Figure 2.9, i.e. controlled powers of $\hat{U} = e^{i\tau\hat{H}}$ to elementary single and two-qubit gates.

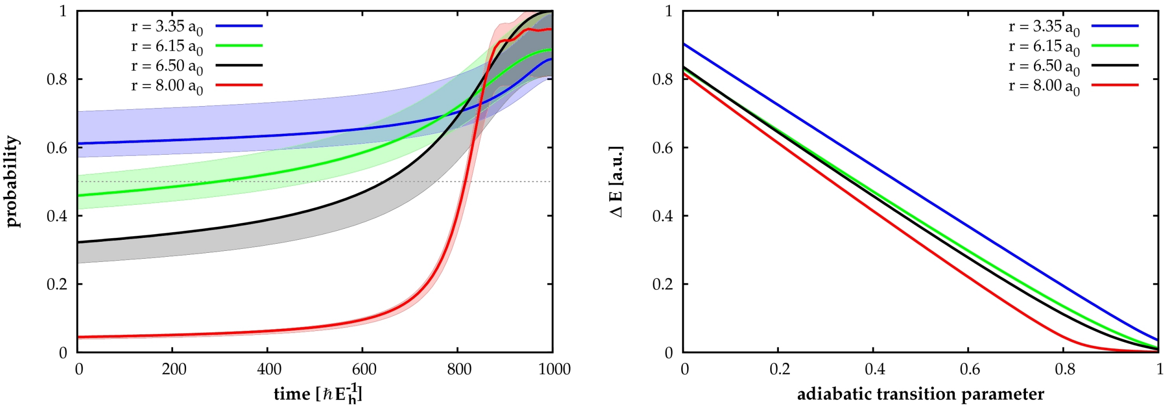

(a)

(b)

Figure 3.1: Adiabatic state preparation (ASP) of the SbH ground state for different internuclear distances. (a) Dependence of the IPEA success probability on time during the ASP (1000 $\hbar E_h^{-1}$ $\approx$ 10^{-14} s). Solid lines correspond to the success probabilities, $|\langle\psi_{\text{ASP}}|\psi_{\text{exact}}\rangle|^2 \cdot \langle 0.81, 1\rangle$ interval is colored. (b) Dependence of the energy gap between the ground and the first excited state on the adiabatic transition parameter s.

For this purpose, it is convenient to express the electronic Hamiltonian in the second quantized form [61]

$$\hat{H} = \sum_{pq} h_{pq} \hat{a}_p^\dagger \hat{a}_q + \frac{1}{2} \sum_{pqrs} g_{pqrs} \hat{a}_p^\dagger \hat{a}_q^\dagger \hat{a}_s \hat{a}_r = \sum_{X=1}^{L} \hat{h}_X, \tag{3.3}$$

where $\hat{a}_p^\dagger$ and $\hat{a}_p$ are fermionic creation and annihilation operators. We suppose that the underlying one-electron basis corresponds to an orthonormal set of e.g. Hartree-Fock spin orbitals $\{\chi_i\}$ and the one and two-electron integrals are defined as

$$h_{pq} \equiv \int \chi_p^*(\mathbf{x}) \left(-\frac{1}{2}\nabla^2 - \sum_A \frac{Z_A}{r_{A,x}} \right) \chi_q(\mathbf{x}) \mathrm{d}\mathbf{x}, \tag{3.4}$$

$$g_{pqrs} \equiv \int \chi_p^*(\mathbf{x_1}) \chi_q^*(\mathbf{x_2}) \frac{1}{r_{1,2}} \chi_r(\mathbf{x_1}) \chi_s(\mathbf{x_2}) \mathrm{d}\mathbf{x_1} \mathrm{d}\mathbf{x_2}. \tag{3.5}$$

Here $\mathbf{x}$ denotes electron spatial and spin coordinates together, ∇^2 is the Laplacian with respect to electron spatial coordinates, r is the distance (between electron and nucleus: $r_{A,x}$ and two electrons: $r_{1,2}$), and Z_A represents a nucleus charge.

The whole summation in (3.3) is formally expressed as a sum of individual terms $\hat{h}_X$. The molecular integrals h_{pq} and g_{pqrs} can be *efficiently* precalculated on a conventional computer

[62] and represent a classical input to the quantum algorithm. In the non-relativistic case they are real-valued, while in the relativistic case they are in general complex.

Since the creation and annihilation operators generally do not commute, the exponential of a Hamiltonian cannot be written as a product of the exponentials of individual $\hat{h}_X$, but a numerical approximation must be used [2]. The first-order Trotter approximation [63] can be expressed as

$$e^{i\tau\hat{H}} = e^{i\tau\sum_{X=1}^{L}\hat{h}_X} = \Big(\prod_{X=1}^{L} e^{i\hat{h}_X\tau/N}\Big)^N + \mathcal{O}(\tau^2/N). \tag{3.6}$$

By choosing $N \geq (\tau^2/\epsilon)$, we can implement $\hat{U}$ within an error tolerance of $\mathcal{O}(\epsilon)$ using $\mathcal{O}(L(\tau^2/\epsilon))$ particular terms $e^{i\hat{h}_X\tau/N}$.

Before discussing the factorization of these terms to elementary quantum gates in Section 3.3.1, we would like to mention the implementation modification we use [24]. Two more external inputs are necessary in our case. These are maximum (E_{max}) and minimum (E_{min}) energies expected in the studied system and we use $\hat{U}$ in the form

$$\hat{U} = e^{i\tau(E_{\text{max}}-\hat{H})}. \tag{3.7}$$

For τ, it holds

$$\tau = \frac{2\pi}{E_{\text{max}} - E_{\text{min}}} \tag{3.8}$$

and the final energy is obtained according to the formula

$$E = E_{\text{max}} - \frac{2\pi\phi}{\tau}. \tag{3.9}$$

The modification mentioned above assures ϕ to be in the interval $\langle 0, 1)$.

E_{min} and E_{max} can in fact be chosen arbitrarily, but one must be sure that the calculated energy is within this interval, otherwise one would end up with a nonphysical energy, due to the periodicity of $e^{2\pi i\phi}$. The maximum energy can be e.g. the upper bound provided by any classical variational (*polynomially* scaling) method, techniques for calculation of lower bounds [64, 65, 66] can on the other hand give the minimum energy. The smaller the interval between them is, the less iterations of IPEA are necessary for the desired precision of E.

Taking $\hat{U}$ in the form (3.7) does not pose any difficulties indeed and as the following circuit equality shows, just one more single qubit rotation is needed.

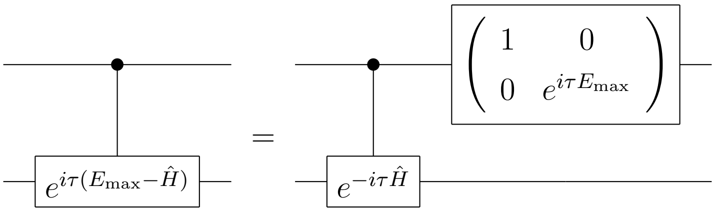
$e^{i\tau(E_{\max}-\hat{H})}$
=
$e^{-i\tau\hat{H}}$
$\begin{pmatrix} 1 & 0 \\ 0 & e^{i\tau E_{\max}} \end{pmatrix}$

3.3.1 Decomposition of unitary propagator to elementary quantum gates

The decomposition of the unitary propagator $e^{i\tau\hat{H}}$ to elementary quantum gates [4, 67, 27] proceeds in the following manner. First, the Jordan-Wigner transform [68] is used to express the fermionic second quantized operators in terms of Pauli σ matrices. The Jordan-Wigner transform has the form

$$\hat{a}_n^\dagger = \left(\bigotimes_{j=1}^{n-1}\sigma_z^j\right)\otimes\sigma_-^n, \quad \hat{a}_n = \left(\bigotimes_{j=1}^{n-1}\sigma_z^j\right)\otimes\sigma_+^n, \tag{3.10}$$

where $\sigma_\pm = 1/2(\sigma_x \pm i\sigma_y)$ and the superscript denotes the qubit on which the matrix operates. The Hamiltonian (3.3) can then be rewritten using strings of σ matrices. Finally, the exponentials of these strings are build up from single qubit gates and CNOTs [28].

We will demonstrate this approach on the one-electron part of the Hamiltonian

$$\hat{H}_1 = \sum_{pq} h_{pq}\hat{a}_p^\dagger\hat{a}_q = \sum_{pp} h_{pp}\hat{a}_p^\dagger\hat{a}_p + \sum_{p>q}\big(h_{pq}\hat{a}_p^\dagger\hat{a}_q + h_{qp}\hat{a}_q^\dagger\hat{a}_p\big). \tag{3.11}$$

In view of the relativistic generalization (Chapter 5), we suppose that molecular integrals are complex-valued. Employing the Jordan-Wigner transform, the diagonal terms can be written as

$$h_{pp}a_p^\dagger a_p = \frac{h_{pp}^{\mathrm{R}}}{2}(\mathbf{1}-\sigma_z^p), \tag{3.12}$$

where h_{pp}^{R} is the real part of h_{pp} [h_{pp}^{I} (the imaginary part) is equal to zero due to the Hermiticity of $\hat{H}$]. For the exponentials it holds

$$e^{i\hat{h}_X\tau/N} = e^{ih_{pp}a_p^\dagger a_p\tau/N} = \begin{pmatrix} 1 & 0 \\ 0 & e^{ih_{pp}\tau/N} \end{pmatrix}^{(p)}. \tag{3.13}$$

The superscript (p) at the matrix denotes the qubit on which the one qubit gate operates.

Similarly, the off-diagonal terms read

$$\begin{aligned} &h_{pq}a_p^\dagger a_q + h_{qp}a_q^\dagger a_p = \\ = \ &\frac{h_{pq}^{\mathrm{R}}}{2}\Big[\sigma_x^p\otimes\big(\sigma_z^{p\to q}\big)\otimes\sigma_x^q + \sigma_y^p\otimes\big(\sigma_z^{p\to q}\big)\otimes\sigma_y^q\Big] + \\ + \ &\frac{h_{pq}^{\mathrm{I}}}{2}\Big[\sigma_y^p\otimes\big(\sigma_z^{p\to q}\big)\otimes\sigma_x^q - \sigma_x^p\otimes\big(\sigma_z^{p\to q}\big)\otimes\sigma_y^q\Big], \end{aligned} \tag{3.14}$$

where $\sigma_z^{p\to q}$ represents the direct product

$$\sigma_z^{p\to q} \equiv \sigma_z^{p+1} \otimes \sigma_z^{p+2} \otimes \ldots \otimes \sigma_z^{q-2} \otimes \sigma_z^{q-1}. \tag{3.15}$$

Note that (3.14) contains the four aforementioned strings of σ matrices.

The exponential of the string of σ_z matrices $\exp[i\tau(\sigma_z \otimes \ldots \otimes \sigma_z)]$ is in fact diagonal in the computational basis with the phase shift $e^{\pm i\tau}$ on the diagonal. The sign of this phase shift depends on the parity of the corresponding basis state ("+" if the number of ones in the binary representation is even, "-" otherwise). The exponential can be implemented with the following circuit [28]

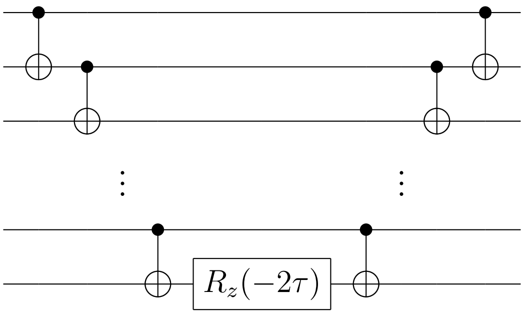

(3.16)

where CNOTs assure the correct sign of the phase shift according to the parity of the state and z-rotations were defined in (1.17).

Due to the following change-of-basis identities [28]

$$\begin{aligned} \sigma_x &= H\sigma_z H^\dagger && (3.17) \\ \sigma_y &= Y'\sigma_z Y'^\dagger, && (3.18) \end{aligned}$$

where

$$Y' = R_x(-\pi/2) = \frac{1}{\sqrt{2}} \begin{pmatrix} 1 & i \\ i & 1 \end{pmatrix}, \tag{3.19}$$

the exponentials

$$\exp\left[\frac{ih_{pq}^{\mathrm{R}}\tau}{2N}\sigma_x^p \otimes \left(\sigma_z^{p\to q}\right) \otimes \sigma_x^q\right]$$

$$\exp\left[\frac{ih_{pq}^{\mathrm{R}}\tau}{2N}\sigma_y^p \otimes \left(\sigma_z^{p\to q}\right) \otimes \sigma_y^q\right]$$

$$\exp\left[\frac{ih_{pq}^{\mathrm{I}}\tau}{2N}\sigma_y^p \otimes \left(\sigma_z^{p\to q}\right) \otimes \sigma_x^q\right]$$

$$\exp\left[\frac{-ih_{pq}^{\mathrm{I}}\tau}{2N}\sigma_x^p \otimes \left(\sigma_z^{p\to q}\right) \otimes \sigma_y^q\right] \tag{3.20}$$

can be implemented with the following circuit pattern

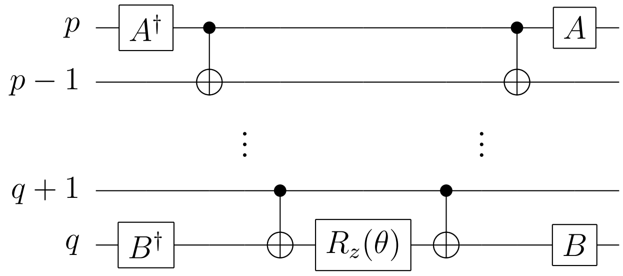

(3.21)

where A and B are for the individual exponentials (3.20) equal to $\{H,H\}$, $\{Y',Y'\}$, $\{Y',H\}$, and $\{H,Y'\}$, respectively, and θ to $-h_{pq}^{\mathrm{R}}\tau/N$, $-h_{pq}^{\mathrm{R}}\tau/N$, $-h_{pq}^{\mathrm{I}}\tau/N$, and $h_{pq}^{\mathrm{I}}\tau/N$, respectively. Note that although the two strings of σ matrices in the first parenthesis in (3.14) commute as do the two strings in the second parenthesis, they do not commute mutually. This, however, is not a complication since the Trotter approximation (3.6) must be employed anyway.

We have demonstrated the decomposition technique for the *direct mapping* approach on the one-electron part of the Hamiltonian. The procedure for the two-electron part is more elaborate, but completely analogous and can be found e.g. in [27].

The overall scaling of the algorithm is given by the scaling of a single controlled action of the unitary propagator without repetitions enforced by the Trotter approximation (3.6). These repetitions increase only the prefactor to the polynomial scaling, not the scaling itself. Also the required precision is limited, about 20 binary digits of ϕ are sufficient to achieve the chemical accuracy [24].

The single controlled action of the exponential of a one-body Hamiltonian (3.11) results in $\mathcal{O}(n^3)$ scaling: there are $\mathcal{O}(n^2)$ different h_{pq} terms and each of them requires $\mathcal{O}(n)$ elementary quantum gates [see the circuit (3.21)]. Since the same decomposition technique applied to the two-electron part of the Hamiltonian gives rise to similar circuit patterns [27], each term g_{pqrs} requires $\mathcal{O}(n)$ elementary quantum gates as well (this in fact holds for general m-body Hamiltonians [67]). The total scaling is thus $\mathcal{O}(n^5)$ [20, 27], where n is the number of molecular spin orbitals and the qFCI achieves an *exponential* speedup over the conventional FCI. This speedup is demonstrated in Figure 3.2.

At this point, we would like to make few remarks. Firstly, we assumed that the initial state preparation is an *efficient* step, as was already mentioned. Secondly, when a quantum chemical method with a scaling worse than $\mathcal{O}(n^5)$ is used for calculation of the initial guess state on a conventional computer, then this classical step becomes a rate determining one. Besides this, the

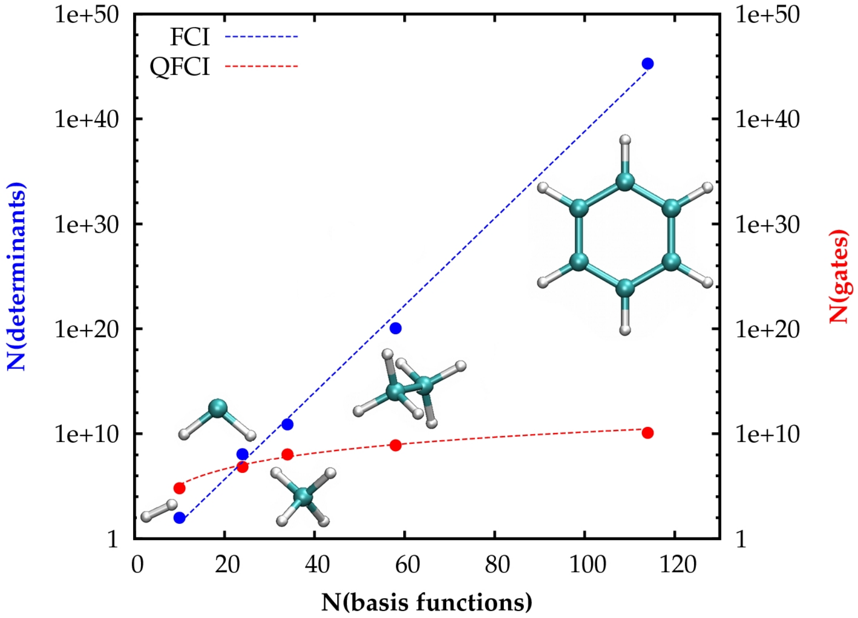

Figure 3.2: The *exponential* speedup of the qFCI over the FCI. In case of the FCI (blue), dependence of the number of Slater determinants in the FCI expansion on the number of basis functions is shown. In case of the qFCI (red), dependence of the number of one and two qubit gates needed for a single controlled action of the unitary operator on the number of basis functions is presented. Points in the graph correspond to the depicted molecules (hydrogen, methylene, methane, ethane, and benzene) in the cc-pVDZ basis set.

classical computation of the integrals in the molecular orbital basis scales as $\mathcal{O}(n^5)$ (due to the integral transformation) as well. We also assumed noise-free qubits and thus did not take into account any quantum error correction [33]. Clark et al. studied the resource requirements for a similar, but fault-tolerant computation of the ground state of a one dimensional transverse Ising model [69] on a proposed scalable quantum computing architecture [70]. They showed that due to the exponential scaling of the resource requirements with the desired energy precision as well as due to the Trotter approximation employed, an elaborate error correction is required, which leads to a huge increase of the computational time. They also gave the values of the experimental parameters (e.g. the physical gate time) needed for acceptable computational times. However, the question of reducing the resource requirements needed for fault tolerant qFCI computations is still open and undergoes an active research.

4 Non-relativistic example: methylene molecule

The following chapter deals with numerical simulations of the qFCI energy calculations of methylene molecule whose goal was to demonstrate the functionality and limitations of the proposed qFCI method. The simulations were carried out on a conventional computer using our own C++ quantum computer simulator code. This chapter is largely based on our article published in the *Journal of Chemical Physics* [24].

4.1 Introduction

Methylene molecule (CH_2) in a minimal basis set (STO-3G) is a simple, yet computationally interesting system suitable for simulations and testing of the qFCI algorithm. CH_2 molecule is well known for the multireference character of its lowest-lying singlet electronic state ($\tilde{a}\ {}^1A_1$) and is often used as a benchmark system for testing of newly developed computational methods (see e.g. [71, 72, 73, 74]). When using the STO-3G basis set, the total number of molecular (spin)orbitals is 7(14). We therefore work with 15 qubits in the direct mapping approach (one qubit is needed in the read-out part of the register). The complexity of simulations of the qFCI on conventional computers scales exponentially, as the complexity of the classical FCI, but with an order of magnitude larger prefactor [12]. Nevertheless, this system is still computationally feasible and due to its properties an excellent candidate for one of the first benchmark simulations.

Our aim was to verify the applicability of the qFCI to the ground as well as excited states exhibiting multireference character. We accordingly simulated the qFCI energy calculations of the four lowest-lying electronic states of CH_2: $\tilde{X}\ {}^3B_1$, $\tilde{a}\ {}^1A_1$, $\tilde{b}\ {}^1B_1$, and $\tilde{c}\ {}^1A_1$. For CH_2 at the equilibrium geometry, the ground electronic state is not a closed-shell singlet, but a triplet state ($\tilde{X}\ {}^3B_1$) with the electronic configuration

$$(1a_1)^2(2a_1)^2(1b_2)^2(3a_1)(1b_1). \tag{4.1}$$

The closed-shell singlet state ($\tilde{a}\ {}^1A_1$), which can be qualitatively described by the electronic configuration

$$(1a_1)^2(2a_1)^2(1b_2)^2(3a_1)^2, \tag{4.2}$$

is the first excited state. This state exhibits a multireference character with the second important configuration

$$(1a_1)^2(2a_1)^2(1b_2)^2(1b_1)^2. \tag{4.3}$$

The contribution of both closed-shell configurations becomes equal at linear geometries. The third electronic state ($\tilde{b}\ ^1B_1$) has the same spatial orbital configuration (4.1) as the ground state, but with singlet-coupled open shell electrons. The fourth electronic state ($\tilde{c}\ ^1A_1$) is represented by the same two configurations as the $\tilde{a}\ ^1A_1$ state but the amplitudes have the same sign and the amplitude of (4.3) is greater than that of (4.1) [this state can be qualitatively described by the configuration (4.3)].

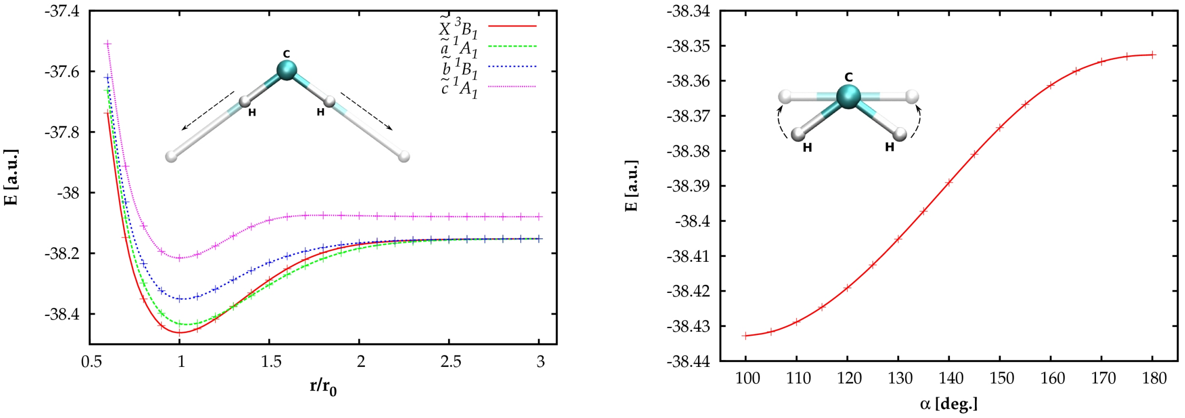

(a)

(b)

Figure 4.1: (a) Energies of the four simulated states of CH_2 for the C-H bond stretching, r_0 denotes the equilibrium bond distance. (b) Energy of $\tilde{a}\ ^1A_1$ state of CH_2 for the H-C-H angle bending, α denotes the H-C-H angle.

We simulated the qFCI energy calculations for C-H bond stretching (both C-H bonds were stretched, Figure 4.1a), and H-C-H angle bending for $\tilde{a}\ ^1A_1$ state (Figure 4.1b). These processes were chosen designedly, since the description of bond breaking is a hard task for many computational methods, and since the H-C-H angle bending leads to a very strong multireference character of the $\tilde{a}\ ^1A_1$ state at linear geometries. The equilibrium geometry of CH_2 molecule was taken from [75] and corresponds to $r_e = 1.1089$ Å and $\alpha_e = 101.89°$). Our work follows up the work by Wang et al. [13], where the authors studied the influence of initial guesses on the performance of the quantum FCI method on two singlet states of water molecule across the bond-dissociation regime. They found out that the Hartree-Fock initial guess is not sufficient for bond dissociation and suggested the use of multi-configurational self consistent field (MCSCF) method (CASSCF in particular). Few configuration state functions added to the initial guess improved the success probability dramatically.

We also used and tested different initial guesses for qFCI calculations. Those denoted as HF guess were composed only from spin-adapted configurations which qualitatively describe certain state: in case of $\tilde{a}\ {}^1A_1$ configuration (4.2), in case of $\tilde{c}\ {}^1A_1$ configuration (4.3), in case of $\tilde{X}\ {}^3B_1$ two triplet-coupled configurations (4.1) (with weights 1/2) and for $\tilde{b}\ {}^1B_1$ the same two configurations but singlet-coupled. Initial guesses denoted as CAS(x,y) guess were based on complete active space configuration interaction (CASCI) calculations with small complete active spaces (more details about the definition of the active spaces will be given further), which contained x electrons in y orbitals. Initial guesses based on CASSCF calculations as in [13] could be used in the same way. To be consistent, we employed the FCI wave functions in a limited active space composed of RHF orbitals, which were also used for the exponential of a Hamiltonian in the qFCI algorithm. Initial guesses were constructed only from the configurations whose absolute values of amplitudes were higher than 0.1. Those constructed from the configurations whose absolute values of amplitudes were higher than 0.2 are denoted as CAS(x,y), tresh. 0.2 guess. All the initial guesses were normalized before simulations.

4.2 Computational details

Similarly as in [12], the exponential of the Hamiltonian operator was implemented as a n-qubit gate. Factorization to elementary single and two-qubit gates was performed only to examine the gate count, but not in the numerical simulations. We also did not take into account any decoherence and thus assumed that the exponential of the Hamiltonian can be obtained with an arbitrary precision by a proper number of repetitions in (3.6). One and two-electron integrals in the MO basis, parametrizing the Hamiltonian (3.3), were obtained using the restricted Hartree-Fock (RHF) orbitals. All *ab initio* calculations (FCI, RHF) were employed with our suite of quantum chemical programs [76].

The phase in IPEA was always computed up to $m = 20$ binary digits. Maximum and minimum expected energies needed for the algorithm were set to $E_{\text{max}} = -37.5$ a.u. and $E_{\text{min}} = -39.0$ a.u. All presented success probabilities correspond to sum of the probabilities of rounding the phase up and down ($P_{\text{tot}} = P_{\text{up}} + P_{\text{down}}$), therefore to probabilities of obtaining the final energy with precision $\approx 1.43 \cdot 10^{-6}$ a.u.

Finally, both of the aforementioned variants of IPEA (**A** and **B**) were tested.

4.3 Results

4.3.1 C-H bond stretching

Results for the C-H bond stretching are summarized in Figures 4.2 - 4.4.

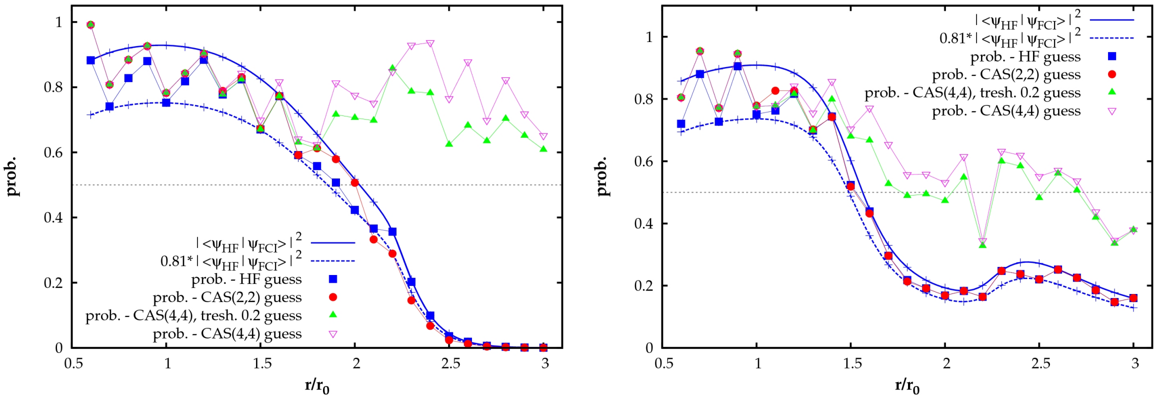

a) $\tilde{a}\ ^1A_1$ state

b) $\tilde{c}\ ^1A_1$ state

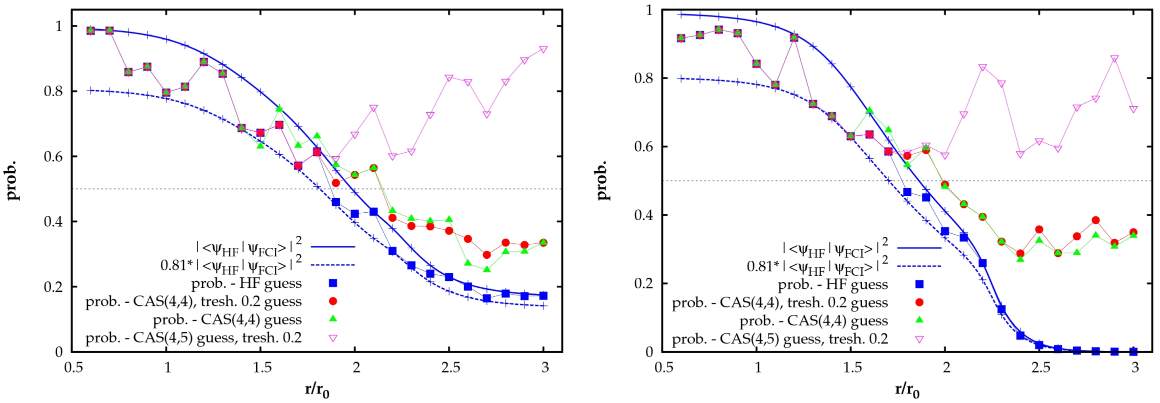

c) $\tilde{X}\ ^3B_1$ state

d) $\tilde{b}\ ^1B_1$ state

Figure 4.2: Success probabilities of the **A** version of IPEA for the four electronic states of CH_2 and different initial guesses, tresh 0.2 means that only configurations with absolute values of amplitudes higher than 0.2 were involved in the initial guess, r_0 denotes the equilibrium bond distance.

Figure 4.2 presents the performance of the **A** version of IPEA with maintaining the second part of the quantum register during all iterations. Subfigures a - d represent the simulations of the energy calculations of the four electronic states: a: $\tilde{a}\ ^1A_1$, b: $\tilde{c}\ ^1A_1$, c: $\tilde{X}\ ^3B_1$, and d: $\tilde{b}\ ^1B_1$. Overlap between the initial HF guess wave function and the exact FCI wave function as well as this overlap scaled by the factor 0.81 [according to (2.22)] are shown. Figure 4.2 also presents the success probabilities of IPEA for the HF initial guess and initial guesses based on

state	**CAS(2,2)**	**CAS(4,4)**	**CAS(4,5)**
$\tilde{a}\,{}^1A_1$	highest occupied MO, lowest unoccupied MO	two highest occupied MOs, two lowest unoccupied MOs	
$\tilde{c}\,{}^1A_1$	highest occupied MO, unoccupied $1b_1$ MO	two highest occupied MOs, unoccupied $1b_1$ MO, lowest unoccupied MO (other than $1b_1$)	
$\tilde{X}\,{}^3B_1$		two highest occupied MOs, unoccupied $1b_1$ MO, lowest unoccupied MO (other than $1b_1$)	two highest occupied MOs, three lowest unoccupied MOs (including $1b_1$)
$\tilde{b}\,{}^1B_1$		two highest occupied MOs, unoccupied $1b_1$ MO, lowest unoccupied MO (other than $1b_1$)	two highest occupied MOs, three lowest unoccupied MOs (including $1b_1$)

Table 4.1: Summary of the complete active spaces (CAS) used for the calculations of initial guesses for IPEA (Figures 4.2 and 4.4), occupation/unoccupation refers to the lowest closed-shell configuration (4.2).

the CASCI calculations with certain small complete active spaces. Definition of these active spaces is complicated by the fact that swapping of molecular orbitals occurs when the C-H bonds are elongated. To maximize the overlap between the initial and the exact wave functions, we constructed the active spaces from the actual highest occupied and the lowest unoccupied molecular orbitals at a given geometry. For $\tilde{X}\ {}^3B_1$, $\tilde{b}\ {}^1B_1$ and $\tilde{c}\ {}^1A_1$, where the $1b_1$ orbital is involved in the qualitative description of the state (at the equilibrium geometry), this orbital was always included in the active space [$1b_1$ orbital which is the LUMO (5th molecular orbital) at the equilibrium geometry becomes the 7th when going to three times elongated C-H bonds]. Definition of the complete active spaces is summarized in Table 4.1. Dotted line in Figure 4.2 corresponding to the probability 0.5 bounds the region where the algorithm can be safely used and the total probability amplified by repeating the whole process.

Figures 4.3 and 4.4 present the performance of the **B** version of IPEA. In this version, the second part of the quantum register is reinitialized at every iteration step. Figures 4.3 and 4.4 demonstrate the success probabilities for different number of such repetitions (11-101). Figure 4.3 shows the results and limits of the HF guess for $\tilde{a}\ {}^1A_1$ state. Figure 4.4 presents the results of the "best" initial guesses in terms of price/performance ratio for all four states.

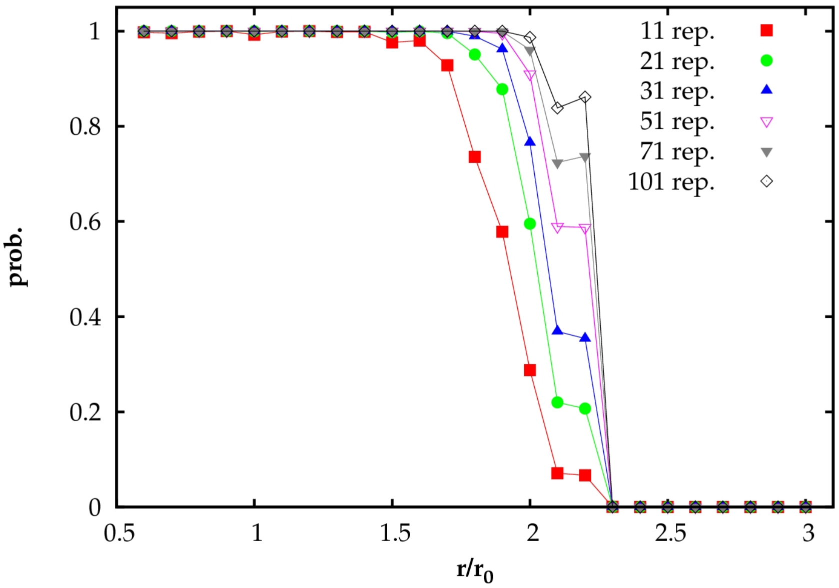

Figure 4.3: Success probabilities of the **B** version of IPEA with HF guess for $\tilde{a}\ ^1A_1$ state and different number of repetitions of individual bit measurements, r_0 denotes the equilibrium bond distance.

4.3.2 H-C-H angle bending

Results for the H-C-H angle bending are summarized in Figures 4.5 and 4.6. Simulations concerning this process involve only the $\tilde{a}\ ^1A_1$ state as this state exhibits a strong multireference character when going to linear geometries. In this case, no swapping of molecular orbitals occurs during the process and the complete active space CAS(2,2) was always constructed from $3a_1$ (HOMO) and $1b_1$ (LUMO) molecular orbitals. Moreover, due to the different symmetry of these orbitals, only two configurations contribute to CAS(2,2) wave function: doubly occupied HOMO [configuration (4.2)] and doubly occupied LUMO [configuration (4.3)]. Both of these configurations have for all values of α (H-C-H angle) absolute values of amplitudes higher than 0.2.

Figure 4.5 presents the results of the **A** version of IPEA. Overlap and scaled overlap of the initial HF guess wave function and the exact FCI wave function is again shown as well as the success probabilities for HF and CAS(2,2), tresh. 0.2 guesses and dotted line bounding the safe region. Performance of the **B** version of IPEA with HF and CAS(2,2), tresh. 0.2 initial guesses is illustrated in Figure 4.6.

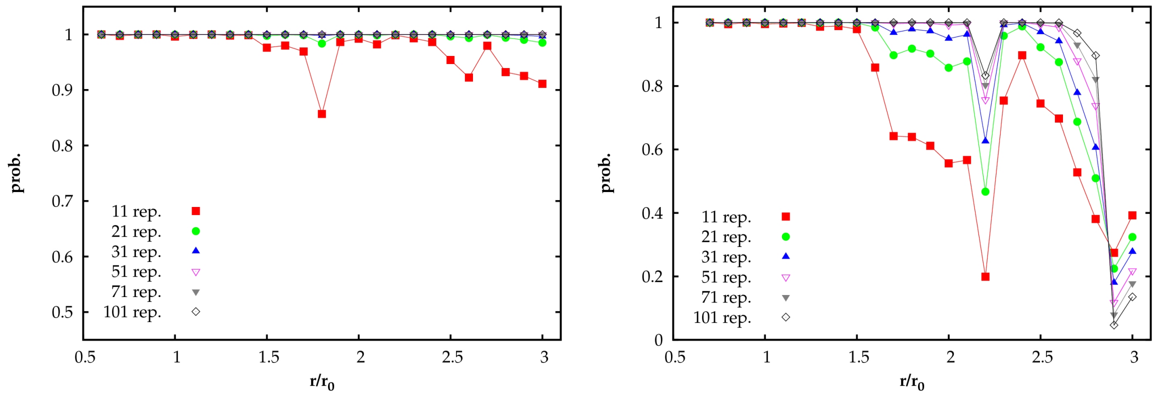

a) $\tilde{a}\ {}^1A_1$ state, CAS(4,4), tresh 0.2 guess b) $\tilde{c}\ {}^1A_1$ state, CAS(4,4), tresh 0.2 guess

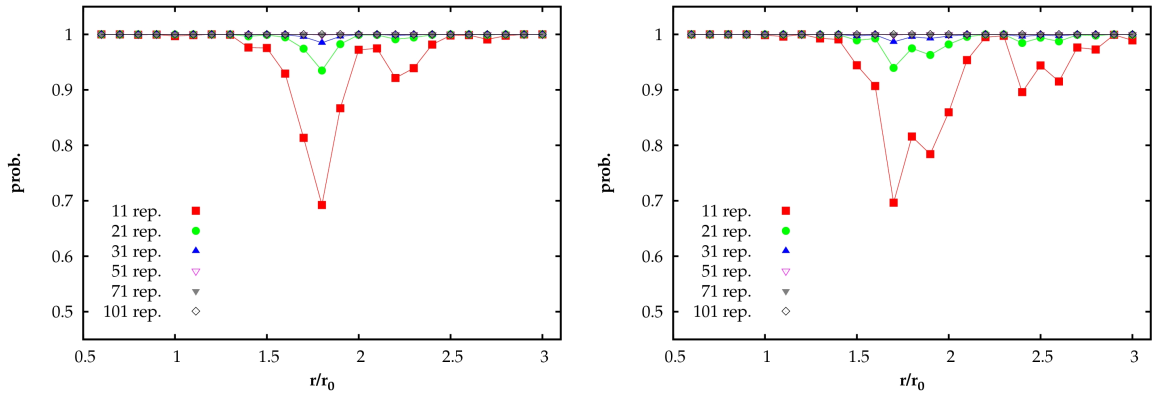

c) $\tilde{X}\ {}^3B_1$ state, CAS(4,5), tresh 0.2 guess d) $\tilde{b}\ {}^1B_1$ state, CAS(4,5), tresh 0.2 guess

Figure 4.4: Success probabilities of the **B** version of IPEA with “best” initial guesses and different number of repetitions of individual bit measurements for all four states, r_0 denotes the equilibrium bond distance.

4.4 Discussion

IPEA - A version

Results of the simulations with **A** version of IPEA numerically confirm that success probabilities always lie in the interval $\left|\langle\psi_{\text{init}}|\psi_{\text{exact}}\rangle\right|^2 \cdot \left(0.81, 1\right\rangle$, depending on the value of the remainder δ (2.21). This algorithm can be safely used when the resulting success probability is higher than 0.5 (as it can then be amplified by repeating the whole process). We would like to note that when studying the applicability of this algorithm, one must monitor the scaled overlap between the initial guess and the exact wave function.

Success probability higher than 0.5 is securely fulfilled with the HF initial guess at the equilibrium geometry for all four simulated states. When going to more stretched C-H bonds

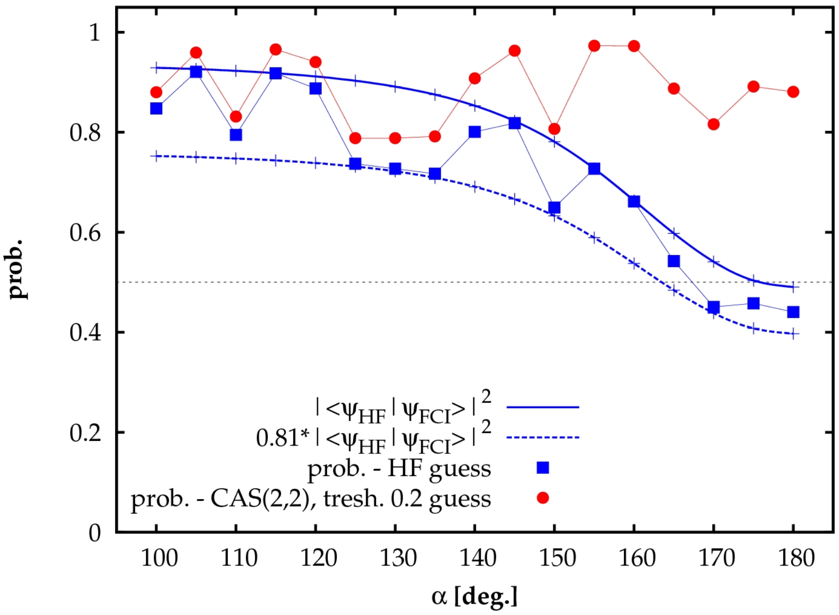

Figure 4.5: Success probabilities of the **A** version of IPEA for the $\tilde{a}\ ^1A_1$ state with HF and CAS(2,2) initial guesses, tresh 0.2 means that only configurations with absolute values of amplitudes higher than 0.2 were involved in the initial guess, α denotes the H-C-H angle.

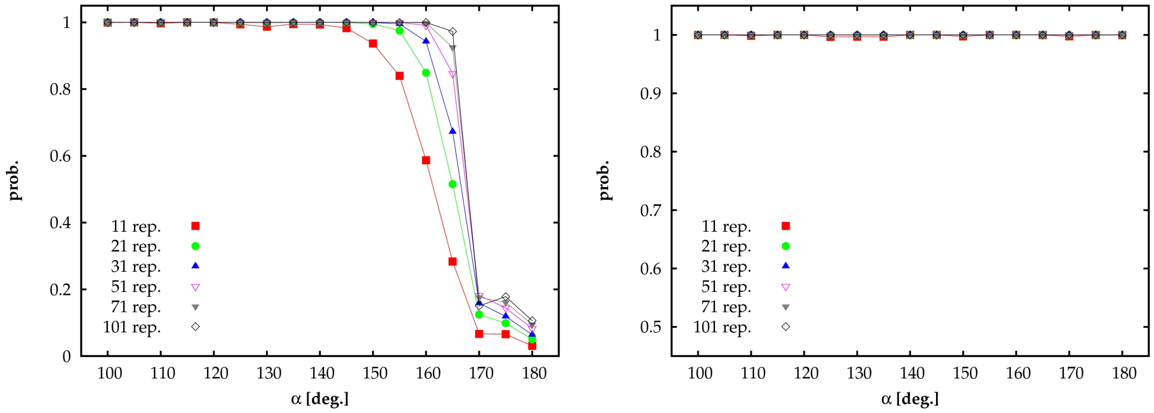

a) HF guess

b) CAS(2,2), tresh. 0.2 guess

Figure 4.6: Success probabilities of the **B** version of IPEA with HF and CAS(2,2), tresh. 0.2 initial guesses and different number of repetitions of individual bit measurements for the $\tilde{a}\ ^1A_1$ state, α denotes the H-C-H angle.

or linear geometry, the RHF initial guess fails. The CAS(2,2) initial guess improves the success probability in case of $\tilde{a}\ ^1A_1$ and $\tilde{c}\ ^1A_1$ states near the equilibrium geometry but in the region of more stretched C-H bonds it also fails. In this region, CAS(4,4) initial guesses must be used. For $\tilde{a}\ ^1A_1$ state, CAS(4,4), tresh. 0.2 guess is sufficient but for $\tilde{c}\ ^1A_1$, even the CAS(4,4) guess fails for few lengths of C-H bonds: $r/r_0 = 2.2, 2.8 - 3.0$. For these points of the potential energy surface, where the overlap between the initial guess and the exact wave functions is not high enough, bigger active space should probably be used.

The situation is more difficult for the states of B_1 symmetry ($\tilde{X}\ ^3B_1$, $\tilde{b}\ ^1B_1$) when the C-H bonds are stretched. Here even CAS(4,4) initial guess fails and bigger active space - CAS(4,5) - must be used for initial guess state calculations. In STO-3G basis set, this bigger complete active space contains five from the total number of seven molecular orbitals and represents therefore nearly the whole space. For this reason, we performed the classical FCI calculations with the cc-pVDZ basis set (*1s* orbital on the carbon atom was kept frozen to reduce computational demands), where the total number of molecular orbitals is 24 (much more than the number of molecular orbitals in the complete active space), and verified that the overlap between the CAS(4,5) and the exact wave function is sufficiently high, essentially the same as in STO-3G basis set. Apart from the active space size, initial guess states always contained at most 12 configurations, but usually 8 or even less for nearly dissociated molecule. This observation is in agreement with the results of [13], where few configuration state functions added to the initial guess improved the success probability dramatically.

High success probabilities (over 0.8) can on the other hand be obtained with CAS(2,2), tresh. 0.2 initial guess for $\tilde{a}\ ^1A_1$ state during H-C-H angle bending. Initial guess states for this process correspond to only two configurations and are thus very easy to prepare (e.g. according to [4]).

IPEA - B version

This version of IPEA is characteristic by repeated initial state preparation in each iteration and has the disadvantage that no collapsing of the system and improving the overlap between the actual state of the quantum register and the exact wave function occurs. The situation is however not so bad because one does not “fight” against the overlap between the initial guess and unwanted eigenfunctions at every iteration. This would happen only if all binary digits of the phase were opposite to binary digits of the phases of all other eigenstates, which is clearly not possible. Our simulations proved that a relatively small number of repetitions (≈ 51) at each iteration step give nearly unity success probability when modest-size initial guesses are used.

The results with the RHF guesses (Figures 4.3 and 4.6a) nicely show their limits (for $\tilde{a}\ ^1A_1$ state). These are: $r/r_0 = 2.3$ for C-H bond stretching and 170° for H-C-H angle bending. We have chosen the “best” initial guess states in terms of price performance ratio for each of the four electronic states: $\tilde{a}\ ^1A_1$ (C-H bond stretching), $\tilde{c}\ ^1A_1$: CAS(4,4), tresh. 0.2; $\tilde{X}\ ^3B_1$, $\tilde{b}\ ^1B_1$:

CAS(4,5), tresh 0.2; $\tilde{a}\ {}^1A_1$ (H-C-H angle bending): CAS(2,2), tresh. 0.2. They were chosen to contain the minimum number of configurations, yet give high enough success probabilities. These initial guesses performed very well with exception of few points for $\tilde{c}\,{}^1A_1$ state, where a bigger active space is desirable.

We have not simulated the decoherence phenomena and when taking it into account the situation will surely change. Quantum error correction [33] would probably be needed for the **A** version, which would increase the number of required qubits as well as the complexity of the quantum circuit, while **B** version should be more robust.

5 Generalization to the relativistic four component regime

In this chapter, we generalize the proposed qFCI method to the relativistic four component (no-pair) regime. We were indeed motivated by two factors. Firstly, it is well understood that relativistic effects can be very important in chemistry. Secondly, so far only the non-relativistic regime (i.e. Schrödinger equation) has been explored and our algorithm thus represents the first quantum algorithm for relativistic computations of molecular energies. We will show how to efficiently solve the eigenproblem of the Dirac-Coulomb Hamiltonian on a quantum computer and demonstrate the functionality of the proposed procedure by numerical simulations of computations of the spin-orbit splitting in the SbH molecule. We have also proposed quantum circuits with 3 qubits and 9 or 10 CNOTs, which implement the first proof-of-principle relativistic quantum chemical calculation for this molecule, and might be suitable for an experimental realization[1]. The chapter is largely based on our *rapid communication* published in the *Physical Review A* journal [25].

5.1 Relativistic electronic Hamiltonian

It is a well known fact that an accurate description of molecules with heavy elements requires an adequate treatment of relativistic effects [77]. The most rigorous approach [besides the quantum electrodynamics (QED) which is presently not feasible for quantum chemical purposes] is the four component (4c) formalism. Our work is based on the 4c electronic Dirac-Coulomb Hamiltonian (DCH) in the form

$$\hat{H} = \sum_{i=1}^{N} \left[c(\boldsymbol{\alpha}_i \cdot \mathbf{p}_i) + \beta'_i mc^2 - \phi_{nuc} \right] + \sum_{i<j} \frac{1}{r_{ij}} + V_{NN}. \tag{5.1}$$

We work within the Born-Oppenheimer clamped nuclei approximation which allows to factorize out time-dependence of the one-electron problem in the inertial frame fixed by the nuclei. The one-electron operator of the electronic Hamiltonian is accordingly given by the Dirac Hamiltonian in the electrostatic potential ϕ_{nuc} of clamped nuclei. Dirac matrices are defined as

---

[1] Presently we are collaborating with an experimental group of Professor Jiangfeng Du from University of Science and Technology of China (Hefei, China) on an NMR experimental realization of the proposed quantum circuits.

$$\boldsymbol{\alpha} = \begin{pmatrix} 0 & \boldsymbol{\sigma} \\ \boldsymbol{\sigma} & 0 \end{pmatrix} \quad \text{and} \quad \beta = \begin{pmatrix} I_2 & 0 \\ 0 & -I_2 \end{pmatrix}, \tag{5.2}$$

the former in terms of the Pauli spin matrices $\boldsymbol{\sigma}$ (1.14). The relativistic energy scale has been aligned with the non-relativistic one by subtraction of the electron rest mass

$$\beta' = \beta - I_4. \tag{5.3}$$

The full Lorentz-invariant two-electron interaction cannot be written in a simple closed form, so approximation and thus loss of strict Lorentz invariance is in practice unavoidable [78]. In Coulomb gauge the zeroth-order $\mathcal{O}(c^0)$ operator is given by the Coulomb term employed here. The resulting Dirac-Coulomb Hamiltonian covers the major part of the spin-orbit interaction, including two-electron spin-same orbit, as well as scalar relativistic effects. Experience shows that the Coulomb term is enough for most chemical purposes [79], but for highly accurate molecular spectra the Breit (Gaunt) term, carrying the spin-other orbit interaction, is recommended.

We restricted ourselves to Dirac-Coulomb Hamiltonian, but it is without loss of generality sufficient for our purposes, since going to Dirac-Coulomb-Breit Hamiltonian is conceptually straightforward as the inclusion of the corresponding integrals requires a classically polynomial effort.

A fundamental conceptual problem is that the Dirac-Coulomb(-Breit) Hamiltonian has no bound solutions due to the one-electron negative-energy continuum solutions generated by the Dirac Hamiltonian [80]. We adopt the no-pair approximation (NPA), widely used in relativistic quantum chemistry [78], in which the N-particle basis of Slater determinants is constructed from positive-energy bispinors only. This procedure in fact neglects all QED effects, but it is justifiable at the energy scale relevant to chemistry. In particular, the Born-Oppenheimer approximation is expected to have a larger impact than the neglect of QED effects.

We finally note that the Fock space approach to include positronic states within the Dirac-Coulomb(-Breit) Hamiltonian approximation [81, 82] should be tractable on a quantum computer as well, since the direct mapping (including qubits for positrons) covers the whole Fock space generated by a finite basis set.

5.2 Relativistic qFCI algorithm

The use of a 4c relativistic formalism brings in three major computational difficulties compared to the non-relativistic case: (1) working with 4c orbitals (bispinors), (2) complex algebra when molecular symmetry is low, and (3) rather large Hamiltonian matrix eigenvalue problems [due to larger mixing of states than in the non-relativistic (NR) case]. The central objective of this section is to address these problems in regard of an application of a quantum computer and the extension of the qFCI method to the relativistic regime.

We will start the description of the algorithm with a mapping of the relativistic quantum chemical wave function onto a quantum register. The simplest (scalable) NR approach, the direct mapping [12], assigns each spin orbital one qubit ($|0\rangle$ = unoccupied, $|1\rangle$ = occupied, see Section 3.1). The relativistic case is similar due to the NPA. Moreover, because of the time-reversal symmetry of the Dirac equation, bispinors occur in degenerate Kramers pairs [78] denoted A and B (analogy to α and β spin in NR treatment) and the relativistic direct mapping thus dedicates one qubit for bispinor A and one for B. The 4c character of molecular bispinors therefore does not complicate the approach substantially [note that as in the NR case, the Hartree-Fock calculation is done on a classical computer and only the exponentially scaling FCI on a quantum one].

As was already mentioned in Section 3.1, the direct mapping is not optimal in the sense that it maps the whole Fock space of the system on the Hilbert space of qubits. For this reason, different compact mappings have been proposed [12, 13]. In the relativistic case, the most convenient compact mapping is based on a subspace of symmetry-adapted functions employing the double group symmetry.

Assuming the NPA and the empty Dirac picture [78], the relativistic Hamiltonian has the same second quantized structure as the NR one (3.3). One and two-electron integrals can be in contrast to NR ones in general complex. This is in fact no difficulty for a quantum computer, since our working environment is a complex vector space of qubits anyway and we do the exponential of a complex matrix even if the Hamiltonian is real. Moreover, when looking at a decomposition of the exponential of a Hamiltonian, which was sketched for a general complex case in Section 3.3.1, one can see that complex molecular integrals require twice as many gates compared to real ones. Note that complex arithmetic on a classical computer requires four times more operations.

The last of the aforementioned difficulties of the 4c formalism is the size of a Hamiltonian matrix eigenvalue problem. This can be inferred from the observation that a significantly larger number of integrals in the Hamiltonian (3.3) will be non-zero due to the lowering of symmetry induced by the spin-orbit interaction. The loss of spin symmetry can to some extent be alleviated by consideration of the time reversal symmetry. In the Kramers-restricted (KR) approach employed in this work the second-quantized Hamiltonian (3.3) is expressed in terms of a basis of Kramers pairs, that is, orbital pairs ϕ_A and ϕ_B connected by time reversal. Determinants may be characterized by a pseudo-quantum number $M_K = 1/2(N_A - N_B)$, reflecting the different number of A and B bispinors. In the non-relativistic limit the Kramers pairs can be aligned with spin partners such that M_K becomes identical to M_S. However, contrary to the NR limit, determinants with different M_K can mix due to the presence of spin-orbit interaction.

Let's now compare the dimensions of relativistic and non-relativistic Hamiltonian matrices. In the NR case, the Hamiltonian matrix is block diagonal according to M_S. Thus for a closed shell system with n electrons in m orbitals, the number of determinants is

$$N_{\mathrm{NR}} = \begin{pmatrix} m \\ n/2 \end{pmatrix}^2 . \tag{5.4}$$

As was already mentioned, the relativistic Hamiltonian mixes determinants with different M_K values and therefore

$$N_{\mathrm{R}} = \sum_{x=0}^{n} \begin{pmatrix} m \\ x \end{pmatrix} \begin{pmatrix} m \\ n-x \end{pmatrix} = \begin{pmatrix} 2m \\ n \end{pmatrix} . \tag{5.5}$$

Using Stirling's approximation in the form

$$\ln m! \approx \frac{1}{2} \ln\, (2\pi m) + m \ln m - m \qquad \text{for } m \to \infty, \tag{5.6}$$

and setting $m = k \cdot n$, the ratio between the relativistic and non-relativistic number of determinants is given by the expression

$$k_{\mathrm{R/NR}} = \frac{N_{\mathrm{R}}}{N_{\mathrm{NR}}} = \left(\frac{\sqrt{\pi(2k-1)}}{2k} \right) \cdot m^{1/2} \tag{5.7}$$

and thus scales as $\mathcal{O}(m^{1/2})$ in the number of molecular orbitals (bispinors).

When employing the direct mapping on a quantum computer, this problem does not occur, since the Hamiltonian (3.3) then implicitly works with all possible values of M_K. The scaling of the relativistic qFCI method is therefore the same as the NR one, namely $\mathcal{O}(m^5)$ [20, 27] , where m is the number of molecular orbitals (bispinors).

Finally, we would like to note that our algorithm can be used stand-alone or as a subroutine of a property algorithm of Kassal et. al. [15] e.g. for calculations of NMR properties.

5.3 Relativistic example: the SbH molecule

For numerical tests of the algorithm, we have chosen the SbH molecule whose non-relativistic ground state $^3\Sigma^-$ splits due to spin-orbit effects into $X\ 0^+$ and $A\ 1$. In the approximate $\lambda\omega$-projection, these states are dominated by $\sigma_{1/2}^2\pi_{1/2}^2\pi_{3/2}^0$ and $\sigma_{1/2}^2\pi_{1/2}^1\pi_{3/2}^1$ configurations. The splitting is truly of "molecular nature" as it disappears for dissociated atoms. Its experimental value is $\Delta E_{\text{SO}} = 654.97$ cm^{-1} [83].

5.3.1 Computational details

In all our simulations, we used the Dyall triple-zeta + valence correlating functions, total 28s 21p 15d 1f for Sb and cc-pVTZ (from the EMSL basis set library) for H. We, of course, could not manage to simulate the FCI calculations with all electrons in such a large basis. We instead simulated general active space (GAS) KRCI computations [84] with the occupation constraints shown in Table 5.1 giving rise to CI spaces of approximately 29500 determinants. For a balanced description of both states, we optimized the spinors taking an average energy expression (2 electrons in 2 Kramers pairs $\pi_{1/2}$, $\pi_{3/2}$). We worked solely with a compact mapping employing the double-group symmetry (C_{2v}^*) and exponential of the Hamiltonian was again simulated as an n-qubit gate (similarly as in [12, 13, 24]). We used the DIRAC program [85] for calculations of Hamiltonian matrices. The nuclear potential ϕ_{nuc} was generated by finite nuclei using Gaussian charge distributions with exponents chosen according to Ref. [86]. As for methylene molecule, simulations of qFCI computations were performed with our own C++ code. We ran 17 iterations of the IPEA with the difference between maximum and minimum expected energies equal to 0.5 E_h. The success probabilities again correspond to sum of the probabilities of rounding the phase up and down ($P_{\text{tot}} = P_{\text{up}} + P_{\text{down}}$) therefore to the final energy precision $\approx 3.81 \times 10^{-6}$ E_h.

GAS	Min. el.	Max. el.	Shell types
I	0	4	$\sigma_{1/2}$, $\pi_{1/2}$
II	2	4	$\pi_{3/2}$
III	4	4	$\sigma_{1/2}^*$, 43 virtual Kramers pairs

Table 5.1: GAS and occupation constraints for SbH $X\ 0^+$ and $A\ 1$ states CI calculations. The minimum and maximum number of electrons are accumulated values - apply to this and all preceding GA spaces.

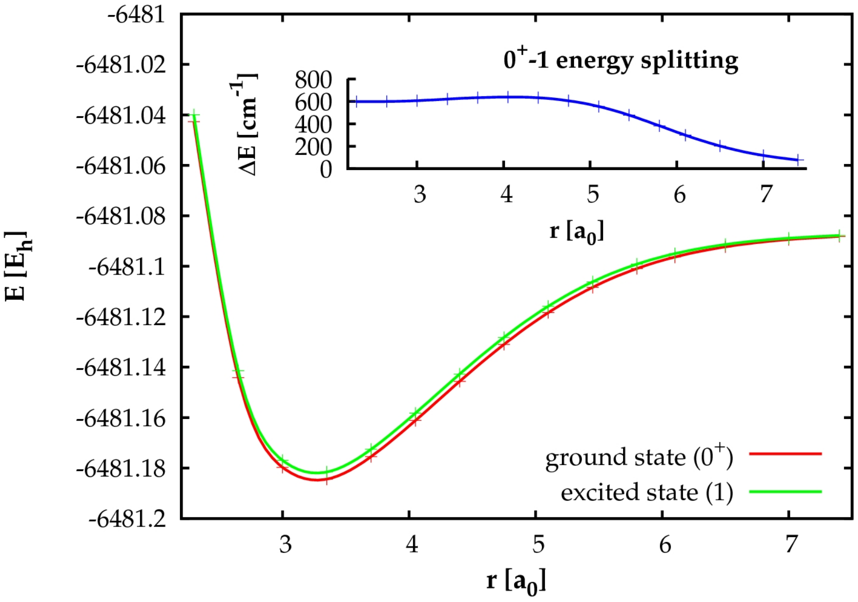

Figure 5.1: Simulated potential energy curves of ground (0^+) and excited (1) states of SbH, and spin-orbit energy splitting. Absolute energies are shifted by $6481\ E_h$.

5.3.2 Results and discussion

Simulated potential energy curves of both states are shown in Figure 5.1. Based on our KRCI setup we obtain a vertical ΔE_{SO} of 617 cm^{-1}. Success probabilities (SPs) of the IPEA version **A** with HF initial guesses ($\sigma_{1/2}^2\pi_{1/2}^2\pi_{3/2}^0$ for the $X\ 0^+$ state and $\sigma_{1/2}^2\pi_{1/2}^1\pi_{3/2}^1$ for $A\ 1$ one) are presented in Figure 5.2. We would like to remind that in this case SPs always lie in the interval $|\langle\psi_{\mathrm{init}}|\psi_{\mathrm{exact}}\rangle|^2 \cdot (0.81, 1\rangle$. Ground state SPs confirm that relativistic states have, due to near degeneracies caused by the spin-orbit coupling, often a stronger multireference character than non-relativistic ones. The upper bound of the SP is less than 0.7 even for the equilibrium geometry and HF initial guesses can in fact be safely used (SP $>$ 0.5, amplification of SP by repetitions) only up to 4.8 a_0. The SPs of the $A\ 1$ state are higher and HF initial guesses can be in a noise-free environment used up to 6 a_0.

The difficulty connected with a low success probability for the $X\ 0^+$ state at longer distances can be overcome either by using more sophisticated (but still polynomially scaling) quantum chemical methods as in our non-relativistic example (see Chapter 4) or by using the ASP method [12]. We simulated $X\ 0^+$ qFCI computations with adiabatically prepared states for different internuclear distances; results are shown in Figures 3.1a and 3.1b in the section devoted to the theory of the ASP. In this case, for computational reasons, we employed complete active space (CAS) KRCI method with a CAS composed of 2 electrons in the highest occupied ($\pi_{1/2}$) and 45 lowest unoccupied Kramers pairs (corresponds to 2116 determinants). It can be seen that for

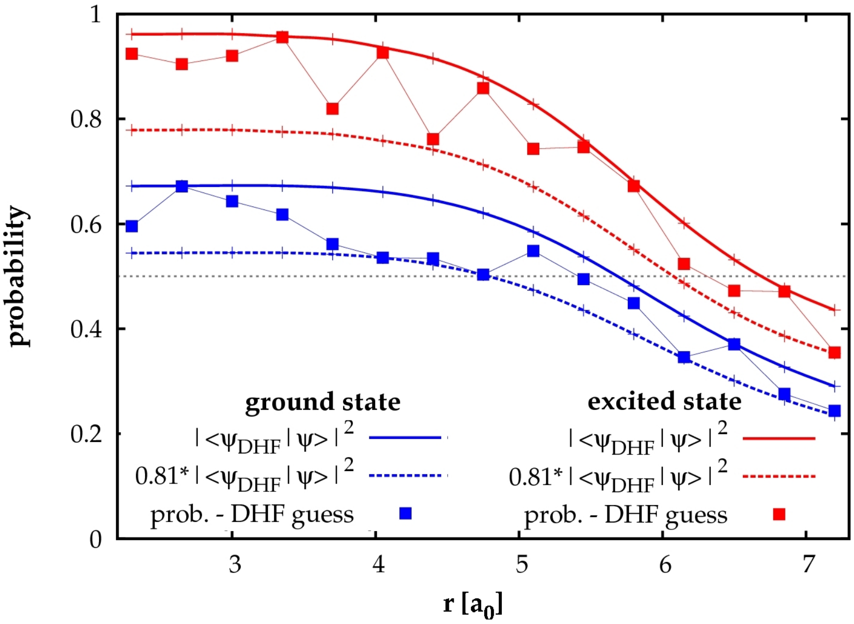

Figure 5.2: SbH ground (0^+) and excited (1) state qFCI success probabilities (SPs) corresponding to HF initial guesses.

$t = 1000\ \hbar E_h^{-1}$, the upper bound of the SP goes safely to unity even for $r = 8\ a_0$.

5.4 Proof-of-principle experiment proposals

Recently, there appeared two papers presenting the first physical implementations of non-relativistic qFCI computations on optical [20] and NMR [21] quantum computers. Correspondingly, we have proposed two candidates for the first relativistic computations on real quantum computers. Our proposals represent “digital (circuit-based) quantum simulations” (DQS) as defined by Bulata and Nori [36]. Conceptually different are “analogue quantum simulations” (AQS), where the evolution of a studied quantum system is mapped to be simulated onto the controlled evolution of the quantum simulator. Recently, Gerritsma et al. used this approach for the proof-of-principle simulation of a one-dimensional Dirac equation with a single trapped ion [87].

Both of our examples represent calculations of SbH $^3\Sigma^-$ ground state spin-orbit splitting. Since one has to employ rather large basis sets (triple-ζ quality) to get a meaningful result, they again are not true FCI calculations, but FCI calculations in a limited CAS. The first one corresponds to a CAS composed of 2 electrons in the highest occupied ($\pi_{1/2}$) and the lowest unoccupied ($\pi_{3/2}$) Kramers pairs [CAS(2,2)]. After the factorization of a Hamiltonian according to the Ω quantum number and taking into account only one of the two degenerate z-projections of Ω (for $\Omega = 1$), the size of the CI space is 2 for the ground state (0^+) and 1 for the excited state (1). The excited state is therefore trivial and the calculation of the ground state is in fact a complete analogue of the already mentioned NR computations [20, 21], because it needs just one qubit for the wave function (2 in total). The controlled single-qubit gate can be decomposed using 2 controlled NOTs (CNOTs) [28]. Calculations with this active space yield $\Delta E_{\mathrm{SO}} = 509$ cm^{-1} computed at the experimental equilibrium bond distance of 3.255 a_0.

The second example represents a 3-qubit experiment (2 qubits for the wave function) and employs a CAS composed of 4 electrons in the $\sigma_{1/2}\pi_{1/2}\pi_{3/2}$ Kramers pairs [CAS(4,3)]. It gives a better value of $\Delta E_{\mathrm{SO}}(518$ cm$^{-1})$ than CAS(2,3). After Ω factorization, the CI space of the excited state has a dimension 3 and that of the ground state 5. Fortunately, near the equilibrium bond distance, the Hamiltonian matrix of the ground state is to a very good approximation block diagonal (ground state energy difference of the order μE_{h}), coupling only 3 configurations ($\sigma^2_{1/2}\pi^2_{1/2}\pi^0_{3/2}$, $\sigma^2_{1/2}\pi^0_{1/2}\pi^2_{3/2}$, and $\sigma^0_{1/2}\pi^2_{1/2}\pi^2_{3/2}$). If we take into account only these configurations, both states can be encoded by two qubits.

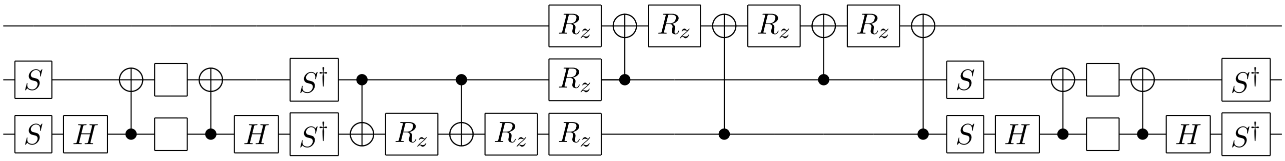

Figure 5.3: Scheme of a circuit corresponding to CAS(4,3) calculations on SbH. Empty squares represent generic single-qubit gates. R_z gates are without angle specification. For derivation, details, and all the parameters, see Appendix B.

We used the *Quantum Shannon Decomposition* (QSD) technique [58] and decomposed the controlled action of a two-qubit $\exp(i\tau\hat{H})$. QSD is known to decompose a generic three-qubit gate with the least number of CNOTs (20). A minimal number of CNOTs is very important as their implementations are orders of magnitude more difficult than single-qubit gates. We found a circuit with 9 CNOTs which is not universal in the sense that the decomposition must be done for all powers of U individually, or a universal 10-CNOT-circuit. The structure of this circuit is shown in Figure 5.3. The controlled action of nth power of U is simply done by multiplication of the angles of R_z rotations by n. Details of the decomposition and also all parameters important for a possible experimental realization which correspond to the calculations at internuclear distance 3.255 a_0 can be found in Appendix B. The proposed experiments are undoubtedly a challenge for different realizations of quantum computation. We regard experimental verification of the usage of HF initial guesses in a realistic noisy environment and also the performance of both versions of IPEA (**A** and **B**) as very interesting.

6 Conclusions

This thesis summarizes our work on the development and simulation of quantum algorithms for quantum chemical problems. To be more concrete, we dealt with the development of quantum algorithms for non-relativistic as well as relativistic full configuration interaction molecular energy calculations that are known to be very computationally demanding on a conventional computer. Quantum computers, on the other hand, offer an *exponential* speedup in this case and promise that *exact* energy calculations of large molecules may be doable in future.

The thesis starts with an introduction to the field of quantum computation that should make the topic comprehensible also for readers without the corresponding background. Afterwards, the details of the quantum FCI algorithm with $\mathcal{O}(n^5)$ scaling and our modifications are presented. Between the most important contributions belongs the suggestion of so called **B** version of the iterative phase estimation algorithm (IPEA) with repeated initial state preparation, which does not require a long coherence time and should thus be a better candidate for the first real larger-scale quantum FCI calculations.

The functionality of the proposed algorithms has been verified by numerical simulations of ground as well as excited state energy calculations of the methylene molecule that exhibits a multireference character. We have demonstrated that energies at the equilibrium geometry are accessible with RHF initial guesses, which are easy to prepare. CASCI initial guess states with small complete active spaces composed of relatively few configurations (≈ 10) are sufficient even for a nearly dissociated molecule to achieve the probability amplification regime of the IPEA algorithm. We should note that all the simulations were performed with our own simulator of a quantum computer (C++ code).

We have further generalized the quantum FCI method to the relativistic four component (no-pair) regime and presented so far the first quantum algorithm for relativistic computations. This algorithm not only achieves an *exponential* speedup over its classical counterpart, but also has the same cost (in terms of scaling) as its non-relativistic analogue. We have proved its functionality by numerical simulations of calculations of the spin-orbit splitting in the SbH molecule. Motivated by the first non-relativistic proof-of-principle experimental realizations [20, 21, 22] that are very promising, we have proposed and designed the first small-scale experimental realizations of relativistic quantum FCI computations. At the moment, we collaborate with an experimental group on their realization.

Hopefully, technical problems connected with a physical realization of quantum computing devices will be solved at some point in the future and exact quantum chemical calculations and simulations of large molecules that are not feasible on conventional computers will belong to the first practical applications of larger-scale quantum computers, leading for example to efficient theoretical design of new drugs or materials.

Appendices

A Probability analysis of the phase estimation algorithm

In this Appendix, we discuss in more detail how the PEA reveals a good estimator of the phase ϕ with high probability [54].

The state of the read-out part of the quantum register after the application of controlled powers of $\hat{U}$, which we here denote as $|\nu\rangle$, can be written as (see Eq. 2.19)

$$|\nu\rangle = \frac{1}{\sqrt{2^m}} \sum_{k=0}^{2^m-1} e^{2\pi i k\phi} |k\rangle. \tag{A.1}$$

The role of the QFT is to perform the transformation

$$|\nu\rangle \longrightarrow |\psi\rangle, \tag{A.2}$$

where ψ is a non-negative integer and $\psi/2^m$ is a good estimator for ϕ with high probability. Since the action of the inverse quantum Fourier transform can be expressed as (see Eq. 2.2)

$$\hat{U}_{\text{QFT}^\dagger}|k\rangle = \frac{1}{\sqrt{2^m}} \sum_{j=0}^{2^m-1} e^{-2\pi i jk/2^m} |j\rangle, \tag{A.3}$$

we can write

$$\begin{aligned}
\hat{U}_{\text{QFT}^\dagger}|\nu\rangle &= \frac{1}{\sqrt{2^m}} \sum_{k=0}^{2^m-1} e^{2\pi i k\phi} \left(\frac{1}{\sqrt{2^m}} \sum_{j=0}^{2^m-1} e^{-2\pi i jk/2^m} |j\rangle \right), & \text{(A.4)}\\
&= \frac{1}{2^m} \sum_{k=0}^{2^m-1} \sum_{j=0}^{2^m-1} e^{2\pi i k(\phi - j/2^m)} |j\rangle, & \text{(A.5)}\\
&= \sum_{j=0}^{2^m-1} \left(\frac{1}{2^m} \sum_{k=0}^{2^m-1} e^{2\pi i k(\phi - j/2^m)} \right) |j\rangle. & \text{(A.6)}
\end{aligned}$$

The probability of measuring a particular outcome j is

$$p_j = \left| \frac{1}{2^m} \sum_{k=0}^{2^m-1} e^{2\pi i k(\phi - j/2^m)} \right|^2. \tag{A.7}$$

When ϕ can be expressed exactly with m bits, i.e. $j = 2^m\phi$

$$p_j(\phi = j/2^m) = \left|\frac{1}{2^m}\sum_{k=0}^{2^m-1} e^{2\pi i k(\phi - j/2^m)}\right|^2 = \left|\frac{1}{2^m}\sum_{k=0}^{2^m-1} 1\right| = 1 \tag{A.8}$$

and we reveal the exact phase with unity probability.

When ϕ cannot be expressed with m bits, the closest estimators correspond to either rounding down: $j/2^m = \tilde{\phi}$, or rounding up: $j/2^m = \tilde{\phi} + 2^{-m}$ (see Eq. 2.21). Equation (A.7) can be simplified in the following way [54]

$$p_j = \frac{1}{2^{2m}}\frac{\sin^2(\pi(2^m\phi - j))}{\sin^2(\pi(\phi - j/2^m))}, \tag{A.9}$$

and for probabilities P_{down} and P_{up} thus holds

$$\begin{aligned} P_{\text{down}} = p_j(j/2^m = \tilde{\phi}) &= \frac{1}{2^{2m}}\frac{\sin^2(\pi\delta)}{\sin^2(\pi\delta 2^{-m})}, & \text{(A.10)} \\ P_{\text{up}} = p_j(j/2^m = \tilde{\phi} + 2^{-m}) &= \frac{1}{2^{2m}}\frac{\sin^2(\pi(1-\delta))}{\sin^2(\pi(1-\delta)2^{-m})}. & \text{(A.11)} \end{aligned}$$

The function plots for $m = 20$ are shown in Figure 2.7. The total success probability P decreases monotonically for increasing m and in the limit $m \longrightarrow \infty$, the lower bound reads

$$P(\delta = 1/2) = P_{\text{down}}(\delta = 1/2) + P_{\text{up}}(\delta = 1/2) = \frac{4}{\pi^2} + \frac{4}{\pi^2} > 0.81. \tag{A.12}$$

B Design of a quantum circuit for SbH proof-of-principle computation

In this Appendix, motivated by designing a non-trivial proof-of-principle relativistic experiments (see Section 5.4), we construct a quantum circuit which corresponds to the controlled action of powers of $U = e^{i\tau\hat{H}}$ on a CI space of dimension 3. For this case, we need two qubits to encode the quantum chemical wave function and U has a block diagonal structure with 3×3 block of an exponential of a Hamiltonian and unity on a diagonal to complete the vector space of two qubits.

We use the *Quantum Shannon Decomposition* technique of Shende et. al. [58]. It turns out to be very useful to generalize the concept of controlled gates to quantum multiplexors. A quantum multiplexor is a quantum conditional which acts on target qubit(s) in a different way, according to the state of select qubit(s). If the select qubit is the most significant one, then it has the following matrix form

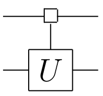

$$= \begin{pmatrix} U_0 & 0 \\ 0 & U_1 \end{pmatrix}. \tag{B.1}$$

It performs U_0 on the target qubit if the select qubit is $|0\rangle$ and U_1 if the select qubit is $|1\rangle$. A controlled gate is a special case where $U_0 = I$. More generally, if U is a quantum multiplexor with s select qubits and t target qubits and the select qubits are most significant, the matrix of U will be block diagonal, with 2^s blocks of size $2^t \times 2^t$.

A controlled 2-qubit U (c-U_{2q}) is a special case of multiplexed U and can be decomposed in the following way [58]

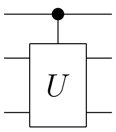

=

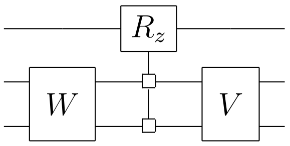

(B.2)

The multiplexed z-rotation in the middle of the circuit on the right-hand side (at this stage without angle specification) is in fact a diagonal matrix with second half of a diagonal equal to a Hermitian conjugate of the first one. The circuit (B.2) corresponds to the matrix equation

$$\begin{pmatrix} I & \\ & U \end{pmatrix} = \begin{pmatrix} V & \\ & V \end{pmatrix} \begin{pmatrix} D & \\ & D^\dagger \end{pmatrix} \begin{pmatrix} W & \\ & W \end{pmatrix}. \tag{B.3}$$

Note that right in the equation means left in the circuit as the time in a circuit flows from the left to the right.

We then have

$$\begin{aligned} I &= VDW, & \text{(B.4)} \\ U &= VD^\dagger W, & \text{(B.5)} \\ U^\dagger &= VD^2V^\dagger. & \text{(B.6)} \end{aligned}$$

A single-multiplexed R_z gate (with angle ϕ_0 for $|0\rangle$ state of a select qubit and ϕ_1 for $|1\rangle$) can be implemented with the following circuit

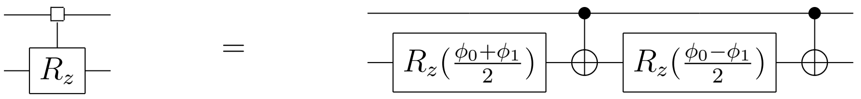
R_z
=
$R_z(\frac{\phi_0+\phi_1}{2})$
$R_z(\frac{\phi_0-\phi_1}{2})$

, (B.7)

since σ_x gates on both sides of R_z turn over the direction of the R_z rotation (see Eq. 1.31). If we use this approach for demultiplexing the R_z gate in (B.2), we end up (after some simple circuit manipulations) with the following circuit for c-U_{2q}

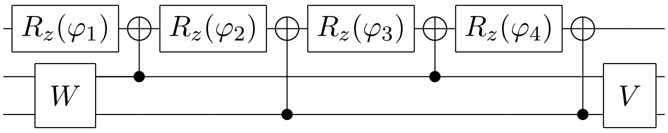

(B.8)

where

$$\begin{aligned} \varphi_1 &= \frac{1}{4}(\phi_{00} + \phi_{01} + \phi_{10} + \phi_{11}), \\ \varphi_2 &= \frac{1}{4}(\phi_{00} + \phi_{01} - \phi_{10} - \phi_{11}), \\ \varphi_3 &= \frac{1}{4}(\phi_{00} - \phi_{01} - \phi_{10} + \phi_{11}), \\ \varphi_4 &= \frac{1}{4}(\phi_{00} - \phi_{01} + \phi_{10} - \phi_{11}). \end{aligned} \tag{B.9}$$

Individual ϕ's in (B.9) can be extracted from the diagonal of D, which has the form: diag($e^{-i\phi_{00}}$,$e^{-i\phi_{01}}$,$e^{-i\phi_{10}}$,$e^{-i\phi_{11}}$).

We would like to emphasize that this is not intended to be a decomposition technique for general U's, as it itself requires a classical diagonalization of $U^\dagger$, see (B.6). A general *efficient* decomposition of an exponential of a Hamiltonian to elementary gates is known only for the direct mapping [20, 27]. But this mapping is not suitable for small scale experiments due to the relatively high number of required qubits and operations thereon. Our aim was in fact to prepare the ground for a first *non-trivial* (more than one qubit in the quantum chemical part of the register) experimental realization of (relativistic) quantum chemical computation on a quantum computer.

Because V belongs to the group **O**(4) (matrix of eigenvectors of a symmetric matrix), it can be decomposed using only two CNOT gates [88]:

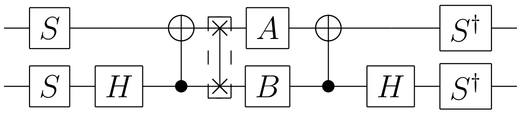

(B.10)

H and S are standard Hadamard and phase gates and A, B are generic single qubit gates that can be further decomposed e.g. by Z-Y decomposition (1.22). There is a highlighted swap gate in (B.10) which should be applied only if the determinant of V is equal to -1 [88].

The matrix W, on the other hand, is not real as it is equal to $D^\dagger V^\dagger$ (B.4) and can be implemented using three CNOT gates (see e.g. [88, 89]). The total count is thus 9 CNOTs.

The disadvantage of the aforementioned scheme is that W must be decomposed for each power of U individually. If we separate W to $V^\dagger$ and $D^\dagger$, $V^\dagger$ is the same for all powers of U (eigenvectors don't change) and $D^\dagger$ can be up to a non-measurable global phase implemented with the following circuit

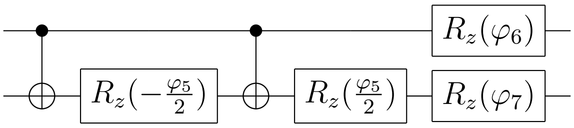

(B.11)

where

$$
\begin{aligned}
\varphi_5 &= \frac{1}{2}(\phi_{00} - \phi_{01} - \phi_{10} + \phi_{11}),\\
\varphi_6 &= \frac{1}{4}(-\phi_{00} - \phi_{01} + \phi_{10} + \phi_{11}),\\
\varphi_7 &= \frac{1}{2}(-\phi_{00} + \phi_{01}).
\end{aligned}
\tag{B.12}
$$

The circuit for $V^\dagger$ is the same as for V (B.10), merely A is replaced by $B^\dagger$ and B by $A^\dagger$.

The presented 10-CNOT-circuit is universal for all powers of U, the only change one has to do is to multiply the angles of R_z rotations in (B.8) and (B.11) according to the power of U, e.g. by 2 for the second power.

Table B.1 summarizes the circuit parameters for SbH ground as well as excited state calculations described in Section 5.4. Notice that ϕ_{11} is zero in both cases by construction. To

	Ground state (0^+)	Excited state (1)
ϕ_{00}	-1.01642278	-1.00656763
ϕ_{01}	-0.68574813	-0.18597924
ϕ_{10}	0.69657237	-0.39129153
ϕ_{11}	0	0
β	0.73125768	-0.00680941
γ	-0.10311594	2.21832498
δ	-0.12107336	-3.13494247
ΔE_{shift}	-6477.89247780	-6477.89247780

Table B.1: Circuit parameters: rotation angles $\phi_{ij}, i, j \in \{0, 1\}$ (B.9,B.12), Z-Y decomposition parameters of A, B (B.10) and energy shifts (core energy + nuclear repulsion) for CAS(4,3) calculations of 0^+ and 1 states of SbH.

complete the vector space of two qubits, we in fact added one eigenvalue of the Hamiltonian equal to zero. Other simplification, which originates from the block diagonal structure of U, is that the A and B matrices in the decomposition of V (B.10) differ only by a global phase. Because the global phase is not measurable, we present just the angles of rotations. Moreover, only the parameters corresponding to A and B are shown. Going to their Hermitian conjugates means swapping β and δ and changing their signs.

For the excited state, the determinant of V is equal to -1 and therefore the swap gate in (B.10) has to be applied. Since we took Hamiltonian matrices from the DIRAC program [85], the parameters in Table B.1 refer to the difference between the total energy and core energy + nuclear repulsion (ΔE_{shift}). The presented method with the parameters from Table B.1 implements the exponential $e^{i\tau\hat{H}}$, as was already mentioned. However, in our version of the algorithm, we in fact need $e^{-i\tau\hat{H}}$ (see Section 3.3). The obtained phase therefore corresponds to the negative of the energy, for which guesses $E_{\text{max}} = 3.5$ and $E_{\text{min}} = 2.0$ corresponding to the maximum and minimum expected energies were used.

We don't give any explicit proof that the *Quantum Shannon decomposition* is optimal in the number of CNOT gates for the specific case of block diagonal c-U_{2q}. However, this conjecture is supported by the fact that we also implemented the Group Leaders Optimization Algorithm (GLOA) of Dashkin and Kais [57] and unsuccessfully tried to find a better circuit (in terms of number of controlled operations) with a fidelity error smaller than 0.01.

List of shortcuts

FCI	...	full configuration interaction
qFCI	...	quantum full configuration interaction
QFT	...	quantum Fourier transform
FFT	...	fast Fourier transform
QEC	...	quantum error correction
WHT	...	Walsh-Hadamard transform
PEA	...	phase estimation algorithm
IPEA	...	iterative phase estimation algorithm
MCSCF	...	multi-configurational self consistent field
CASSCF	...	complete active space self consistent field
CASCI	...	complete active space configuration interaction
HOMO	...	highest occupied molecular orbital
LUMO	...	lowest unoccupied molecular orbital
QED	...	quantum electrodynamics
DCH	...	Dirac-Coulomb Hamiltonian
NPA	...	no-pair approximation
NR	...	non-relativistic
GAS	...	general active space
KR	...	Kramers restricted
KRCI	...	Kramers restricted configuration interaction
SP	...	success probability
ASP	...	adiabatic state preparation
QSD	...	quantum Shannon decomposition
NMR	...	nuclear magnetic resonance
P	...	polynomial time
NP	...	nondeterministic polynomial time
BPP	...	bounded-error probabilistic polynomial time
BQP	...	bounded-error quantum polynomial time
QMA	...	quantum Merlin Arthur

Bibliography

[1] R. P. Feynman, “Simulating physics with computers,” *Int. J. Theor. Phys.*, vol. 21, pp. 467–488, 1982.

[2] S. Lloyd, “Universal quantum simulators,” *Science*, vol. 273, p. 1073, 1996.

[3] C. Zalka, “Simulating quantum systems on a quantum computer,” *Proc. R. Soc. London Ser. A*, vol. 454, pp. 313–322, 1998.

[4] G. Ortiz, J. E. Gubernatis, E. Knill, and R. Laflamme, “Quantum algorithms for fermionic simulations,” *Phys. Rev. A*, vol. 64, p. 022319, 2001.

[5] R. Somma, G. Ortiz, J. E. Gubernatis, E. Knill, and R. Laflamme, “Simulating physical phenomena by quantum networks,” *Phys. Rev. A*, vol. 65, p. 042323, 2002.

[6] D. S. Abrams and S. Lloyd, “Simulation of many-body fermi systems on a universal quantum computer,” *Phys.Rev.Lett.*, vol. 79, pp. 2586–2589, 1997.

[7] P. W. Shor, “Algorithms for quantum computation: Discrete logarithms and factoring,” in *Proceedings of 35th IEEE Symposium on Foundations of Computer Science*, pp. 124–134, IEEE Press, 1994.

[8] P. W. Shor, “Polynomial time algorithms for prime factorization and discrete logarithms on quantum computer,” *SIAM Journal on Computing*, vol. 25, pp. 1484–1509, 1997.

[9] L. K. Grover, “Quantum mechanics helps in searching for a needle in a haystack,” *Phys. Rev. Lett.*, vol. 79, p. 325, 1997.

[10] D. S. Abrams and S. Lloyd, “A quantum algorithm providing exponential speed increase for finding eigenvalues and eigenvectors,” *Phys.Rev.Lett.*, vol. 83, pp. 5162–5165, 1999.

[11] D. A. Lidar and H. Wang, “Calculating the thermal rate constant with exponential speedup on a quantum computer,” *Phys. Rev. E*, vol. 59, pp. 2429–2438, 1999.

[12] A. Aspuru-Guzik, A. D. Dutoi, P. J. Love, and M. Head-Gordon, “Simulated quantum computation of molecular energies,” *Science*, vol. 309, pp. 1704–1707, 2005.

[13] H. Wang, S. Kais, A. Aspuru-Guzik, and M. R. Hoffmann, “Quantum algorithm for obtaining the energy spectrum of molecular systems,” *Phys. Chem. Chem. Phys.*, vol. 10, pp. 5388–5393, 2008.

[14] I. Kassal, S. P. Jordan, P. J. Love, M. Mohseni, and A. Aspuru-Guzik, “Polynomial-time quantum algorithm for the simulation of chemical dynamics,” *Proc. Natl. Acad. Sci.*, vol. 105, pp. 18681–18686, 2008.

[15] I. Kassal and A. Aspuru-Guzik, “Quantum algorithm for molecular properties and geometry optimization,” *J. Chem. Phys.*, vol. 131, p. 224102, 2009.

[16] N. J. Ward, I. Kassal, and A. Aspuru-Guzik, “Preparation of many-body states for quantum simulation,” *J. Chem. Phys.*, vol. 130, p. 194105, 2009.

[17] H. Wang, S. Ashhab, and F. Nori, “Efficient quantum algorithm for preparing molecular-system-like states on a quantum computer,” *Phys. Rev. A*, vol. 79, p. 042335, 2009.

[18] J. Zhu, Z. Huang, and S. Kais, “Simulated quantum computation of global minima,” *Mol. Phys.*, vol. 107, pp. 2015–2023, 2009.

[19] I. Kassal, J. D. Whitfield, A. Perdomo-Ortiz, M. H. Yung, and A. Aspuru-Guzik, “Simulating chemistry using quantum computers,” *Annu. Rev. Phys. Chem*, vol. 62, pp. 185–207, 2011.

[20] B. P. Lanyon, J. D. Whitfield, G. G. Gillett, M. E. Goggin, M. P. Almeida, I. Kassal, J. D. Biamonte, M. Mohseni, B. J. Powell, M. Barbieri, A. Aspuru-Guzik, and A. G. White, “Towards quantum chemistry on a quantum computer,” *Nature Chemistry*, vol. 2, pp. 106–111, 2010.

[21] J. Du, N. Xu, X. Peng, P. Wang, S. Wu, and D. Lu, “NMR implementation of a molecular hydrogen quantum simulation with adiabatic state preparation,” *Phys. Rev. Lett.*, vol. 104, p. 030502, 2010.

[22] Z. Li, M.-H. Yung, H. Chen, D. Lu, J. D. Whitfield, S. Peng, A. Aspuru-Guzik, and J. Du, “Solving quantum ground-state problems with nuclear magnetic resonance,” *Sci. Rep.*, vol. 1, p. 88, 2011.

[23] D. Lu, N. Xu, R. Xu, H. Chen, J. Gong, X. Peng, and J. Du, “Simulation of chemical isomerization reaction dynamics on a NMR quantum simulator,” *Phys. Rev. Lett.*, vol. 107, p. 020501, 2011.

[24] L. Veis and J. Pittner, “Quantum computing applied to calculations of molecular energies: CH_2 benchmark,” *J. Chem. Phys.*, vol. 133, p. 194106, 2010.

[25] L. Veis, J. Višňák, T. Fleig, S. Knecht, T. Saue, L. Visscher, and J. Pittner, “Relativistic quantum chemistry on quantum computers,” *Phys. Rev. A*, vol. 85, p. 030304, 2012.

[26] L. Veis and J. Pittner, “Quantum computing approach to non-relativistic and relativistic molecular energy calculations,” *arXiv:quant-ph/1203.6204v1*, 2012.

[27] J. D. Whitfield, J. Biamonte, and A. Aspuru-Guzik, “Quantum computing resource estimate of molecular energy simulation,” *Mol. Phys.*, vol. 109, pp. 735–750, 2011.

[28] M. A. Nielsen and I. L. Chuang, *Quantum Computation and Quantum Information*. Cambridge University Press, 2000.

[29] D. Deutsch, “Quantum computational networks,” *Proc. R. Soc. A*, vol. 425, pp. 73–90, 1989.

[30] C. Cohen-Tannoudji, B. Diu, and F. Laloe, *Quantum Mechanics, Vol. I.* John Wiley and Sons, New York, 1977.

[31] A. Barenco, C. H. Bennett, R. Cleve, D. P. DiVincenzo, N. Margolus, P. Shor, T. Sleator, J. A. Smolin, and H. Weinfurter, “Elementary gates for quantum computation,” *Phys. Rev. A*, vol. 52, no. 5, pp. 3457–3467, 1995.

[32] P. O. Boykin, T. Mor, M. Pulver, V. Roychowdhury, and F. Vatan, “A new universal and fault-tolerant quantum basis,” *Inf. Process. Lett.*, vol. 75, pp. 101–107, 2000.

[33] F. Gaitan, *Quantum Error Correction and Fault Tolerant Quantum Computing*. CRC Press, 2008.

[34] J. Kempe, A. Kitaev, and O. Regev, “The complexity of the local Hamiltonian problem,” *SIAM JOURNAL ON COMPUTING*, vol. 35, no. 5, pp. 1070–1097, 2006.

[35] W. H. Zurek, “Decoherence and the transition from quantum to classical – revisited,” *arXiv:quant-ph/0306072v1*, 2003.

[36] I. Buluta and F. Nori, “Quantum simulators,” *Science*, vol. 326, pp. 108–111, 2009.

[37] T. D. Ladd, F. Jelezko, R. Laflamme, Y. Nakamura, C. Monroe, and J. L. O'Brien, "Quantum computers," *Nature*, vol. 464, pp. 45–53, 2010.

[38] D. P. DiVincenzo, "The physical implementation of quantum computation," *Fortschr. Phys.*, vol. 48, pp. 771–783, 2000.

[39] B. P. Lanyon, C. Hempel, D. Nigg, M. Müller, R. Gerritsma, F. Zähringer, P. Schindler, J. T. Barreiro, M. Rambach, G. Kirchmair, M. Hennrich, P. Zoller, R. Blatt, and C. F. Ross, "Universal digital quantum simulation with trapped ions," *Science*, vol. 334, pp. 57–61, 2011.

[40] J. L. O'Brien, "Optical quantum computing," *Science*, vol. 318, pp. 1567–1570, 2007.

[41] E. Knill, R. Laflamme, and G. J. Milburn, "A scheme for efficient quantum computation with linear optics," *Nature*, vol. 409, pp. 46–52, 2001.

[42] R. Raussendorf and H. J. Briegel, "A one-way quantum computer," *Phys. Rev. Lett.*, vol. 86, pp. 5188–5191, 2001.

[43] A. Politi, J. C. F. Matthews, and J. L. O'Brien, "Shor's quantum factoring algorithm on a photonic chip," *Science*, vol. 325, p. 1221, 2009.

[44] J. C. F. Matthews, A. Politi, A. Stefanov, and J. L. O'Brien, "Manipulation of multiphoton entanglement in waveguide quantum circuit," *Nature Photon.*, vol. 3, pp. 346–350, 2009.

[45] D. G. Cory, A. F. Fahmy, and T. F. Havel, "Ensemble quantum computing by NMR spectroscopy," *Proc. Natl. Acad. Sci.*, vol. 94, pp. 1634–1639, 1997.

[46] N. A. Gershenfeld and I. L. Chuang, "Bulk spin resonance quantum computation," *Science*, vol. 275, pp. 350–356, 1997.

[47] H. Günther, *NMR Spectroscopy: Basic Principles, Concepts, and Applications in Chemistry, 2nd Edition*. John Wiley and Sons, 1995.

[48] J. A. Jones, "Quanum computing with NMR," *Prog. Nucl. Magn. Reson. Spec.*, vol. 59, pp. 91–120, 2011.

[49] C. A. Ryan, O. Moussa, J. Baugh, and R. Laflamme, "Spin based heat engine: demonstration of multiple rounds of algorithmic cooling," *Phys. Rev. Lett.*, vol. 100, p. 140501, 2008.

[50] C. Negrevergne, T. S. Mahesh, C. A. Ryan, M. Ditty, F. Cyr-Racine, W. Power, N. Boulant, T. Havel, D. G. Cory, and R. Laflamme, "Benchmarking quantum control methods on a 12-qubit system," *Phys. Rev. Lett.*, vol. 96, p. 170501, 2006.

[51] J. I. Cirac and P. Zoller, "Quantum computations with cold trapped ions," *Phys. Rev. Lett.*, vol. 74, p. 4091, 1995.

[52] J. P. Home, D. Hanneke, J. D. Jost, J. M. Amini, D. Leibfried, and D. J. Wineland, "Complete methods set for scalable ion trap quantum information processing," *Science*, vol. 325, pp. 1227–1230, 2009.

[53] R. B. Griffiths and Chi-Sheng Niu, "Semiclassical fourier transform for quantum computation," *Phys. Rev. Lett.*, vol. 76, pp. 3228–3231, 1996.

[54] M. Dobšíček, *Quantum computing, phase estimation and applications*. PhD thesis, Faculty of Electrical Engineering, Czech Technical University in Prague, 2008.

[55] H. Wang, L.-A. Wu, Y. xi Liu, and F. Nori, "Measurement-based quantum phase estimation algorithm for finding eigenvalues of non-unitary matrices," *Phys. Rev. A*, vol. 82, p. 062303, 2010.

[56] M. Dobšíček, G. Johansson, V. Shumeiko, and G. Wendin, "Arbitrary accuracy iterative quantum phase estimation algorithm using a single ancillary qubit: A two-qubit benchmark," *Phys. Rev. A*, vol. 76, p. 030306, 2007.

[57] A. Daskin and S. Kais, "Decomposition of Unitary Matrices for Finding Quantum Circuits: Application to Molecular Hamiltonians," *J. Chem. Phys.*, vol. 134, p. 144112, 2011.

[58] V. V. Shende, S. S. Bullock, and I. L. Markov, "Synthesis of quantum logic circuits," *IEEE Trans. on Computer-Aided Design*, vol. 25, pp. 1000–1010, 2006.

[59] A. Daskin, A. Grama, G. Kollias, and S. Kais, "Universal programmable quantum circuit schemes to emulate an operator," *arXiv:quant-ph/1204.3600v3*, 2012.

[60] E. Fahri, J. Goldstone, S. Gutmann, J. Lapan, A. Lundgren, and D. Preda, "A quantum adiabatic evolution algorithm applied to random instances of an NP-complete problem," *Science*, vol. 292, pp. 472–476, 2001.

[61] A. Szabo and N. Ostlund, *Modern Quantum Chemistry: Introduction to Advanced Electronic Structure Theory*. Dover Publications, 1996.

[62] T. Helgaker, P. Jorgensen, and J. Olsen, *Molecular Electronic-Structure Theory*. Wiley, 2000.

[63] N. Hatano and M. Suzuki, "Quantum annealing and other optimization methods," in *Lecture Notes in Physics*, ch. Finding Exponential Product Formulas of Higher Orders, Springer, Heidelberg, 2005.

[64] N. W. Bazley, "Lower bounds for eigenvalues with application to the helium atom," *Phys. Rev.*, vol. 120, p. 144, 1960.

[65] P.-O. Löwdin, "Studies in Perturbation Theory. IV. Solution of Eigenvalue Problem by Projection Operator Formalism," *J. Math. Phys.*, vol. 3, p. 969, 1962.

[66] P.-O. Löwdin, "Studies in perturbation theory. X. Lower bounds to energy eigenvalues in perturbation-theory ground state," *Phys. Rev. A*, vol. 139, p. 357, 1965.

[67] E. Ovrum and M. Hjorth-Jensen, "Quantum computation algorithm for many-body studies," *arXiv:quant-ph/0705.1928v1*, 2007.

[68] P. Jordan and E. Wigner, "Uber das paulische aquivalenzverbot," *Z. Phys. A*, vol. 47, p. 631, 1928.

[69] C. R. Clark, T. S. Metodi, S. D. Gasster, and K. R. Brown, "Resource Requirements for Fault-Tolerant Quantum Simulation: The Transverse Ising Model Ground State," *Phys. Rev. A*, vol. 79, p. 062314, 2009.

[70] T. S. Metodi, D. D. Thaker, A. W. Cross, F. T. Chong, and I. L. Chuang., "A quantum logic array microarchitecture: Scalable quantum data movement and computation.," in *Proceeding of the 38th Annual IEEE/ACM International Symposium on Microarchitechture*, p. 305, 2005.

[71] J. Pittner, P. Nachtigall, P. Čársky, J. Mášik, and I. Hubač, "Assessment of the single-root multireference Brillouin-Wigner coupled cluster method. Test calculations on CH_2, SiH_2, and twisted ethylene," *J. Chem. Phys.*, vol. 110, pp. 10275–10282, 1999.

[72] F. A. Evangelista, W. D. Allen, and H. F. Schaefer III, "High-order excitations in state-universal and state-specific multireference coupled-cluster theories: Model systems," *J. Chem. Phys.*, vol. 125, p. 154113, 2006.

[73] K. Bhaskaran-Nair, O. Demel, and J. Pittner, "Multireference Mukherjee's Coupled Cluster method with triexcitations in the linked formulation: efficient implementation and applications," *J. Chem. Phys.*, vol. 132, p. 154105, 2010.

[74] O. Demel and J. Pittner, “Multireference Brillouin-Wigner Coupled Clusters Method with Singles, Doubles, and Triples: Efficient Implementation and Comparison with Approximate Approaches,” *J. Chem. Phys.*, vol. 128, p. 104108, 2008.

[75] C. D. Sherrill, M. L. Leininger, T. J. Van Huis, and H. F. Schaefer III, “Structures and vibrational frequencies in the full configuration interaction limit: Predictions for four electronic states of methylene using triple-zeta plus double polarization (tz2p) basis,” *J. Chem. Phys.*, vol. 108, pp. 1040–1049, 1998.

[76] J. Pittner, “*TINY package*, suite of quantum chemical programs written in C++ based on the linear algebra library *LA*: http://www.pittnerovi.com/la.”

[77] B. A. Hess and C. M. Marian, “Relativistic effects in the calculation of electronic energies,” in *Computational Molecular Spectroscopy* (P. Jensen and P. R. Buenker, eds.), pp. 169–219, Sussex: Wiley, 2000.

[78] K. G. Dyall and K. Faegri, *Introduction to Relativistic Quantum Chemistry*. Oxford University Press, 2007.

[79] O. Visser, L. Visscher, P. J. C. Aerts, and W. C. Nieuwpoort, “Relativistic all-electron molecular Hartree-Fock-Dirac- (Breit) calculations on CH_4, SiH_4, GeH_4, SnH_4 and PbH_4,” *Theor. Chim. Acta*, vol. 81, p. 405, 1992.

[80] G. E. Brown and D. G. Ravenhall, “On the interaction of two electrons,” *Proc. Roy. Soc. London A*, vol. 208, pp. 552–559, 1951.

[81] T. Saue and L. Visscher, “Four-component electronic structure methods for molecules,” in *Theoretical Chemistry and Physics of Heavy and Superheavy Elements* (S. Wilson and U. Kaldor, eds.), p. 211, Dordrecht: Kluwer, 2003.

[82] W. Kutzelnigg, “Solved and unsolved problems in relativistic quantum chemistry,” *Chem. Phys.*, vol. 395, pp. 16–34, 2012.

[83] K. Balasubramanian, “Spectroscopic properties and potential energy curves for heavy p-block diatomic hydrides, halides, and chalconides,” *Chem. Rev.*, vol. 89, pp. 1801–1840, 1989.

[84] T. Fleig, J. Olsen, and L. Visscher, “The generalized active space concept for the relativistic treatment of electron correlation. ii. large-scale configuration interaction implementation based on relativistic 2- and 4-spinors and its application,” *J. Chem. Phys.*, vol. 119, p. 2963, 2003.

[85] DIRAC, a relativistic ab initio electronic structure program, Release DIRAC08 (2008), written by L. Visscher, H. J. Aa. Jensen, and T. Saue, with new contributions from R. Bast, S. Dubillard, K. G. Dyall, U. Ekström, E. Eliav, T. Fleig, A. S. P. Gomes, T. U. Helgaker, J. Henriksson, M. Iliaš, Ch. R. Jacob, S. Knecht, P. Norman, J. Olsen, M. Pernpointner, K. Ruud, P. Sałek, and J. Sikkema (see http://dirac.chem.sdu.dk).

[86] L. Visscher and K. G. Dyall, "Dirac-Fock atomic electronic structure calculations using different nuclear charge distributions," *At. Data Nucl. Data Tables*, vol. 67, p. 207, 1997.

[87] R. Gerritsma, G. Kirchmair, F. Zahringer, E. Solano, R. Blatt, and C. F. Roos, "Quantum simulation of the Dirac equation," *Nature*, vol. 463, pp. 68–72, 2010.

[88] F. Vatan and C. Williams, "Optimal quantum circuits for general two-qubit gates," *Phys. Rev. A*, vol. 69, p. 032315, 2004.

[89] V. V. Shende, I. L. Markov, and S. S. Bullock, "Minimal universal two-qubit controlled-not-based circuits," *Phys. Rev. A*, vol. 69, p. 062321, 2004.